

# The radial spreading of volcanic umbrella clouds deduced from satellite measurements

 Fred Prata\*<sup>α,β</sup>,  Andrew T. Prata<sup>γ</sup>,  Rebecca Tanner<sup>δ</sup>,  Roy G. Grainger<sup>ε</sup>,  Mike Borgas<sup>ζ</sup>, and  Thomas J. Aubry<sup>δ</sup>

<sup>α</sup> Aires Pty Ltd, Mount Eliza, Victoria, 3930 Australia.

<sup>β</sup> School of Electrical Engineering, Computing and Mathematical Sciences, Curtin University, Bentley, Perth, WA 6102, Australia.

<sup>γ</sup> CSIRO Environment, Research Way, Clayton, Victoria, 3168 Australia.

<sup>δ</sup> Department of Earth and Environmental Sciences, University of Exeter, Penryn, UK.

<sup>ε</sup> Atmospheric, Oceanic and Planetary Physics, University of Oxford, Oxford OX1 3PU, UK.

<sup>ζ</sup> Yanakie Research Institute, 3670 Meeniyah-Promontory Rd, Yanakie Victoria, 3960 Australia.

## ABSTRACT

Analysis of thermal infrared satellite measurements of umbrella clouds generated by volcanic eruptions suggests that asymptotic gravity current models of the temporal ( $t$ ) radial ( $r$ ) spreading ( $r \sim t^f$ ,  $f < 1$ ) of the umbrella-shaped intrusion do not adequately explain the observations. Umbrella clouds from 13 volcanic eruptions are studied using satellite data that have spatial resolutions of  $\sim 4\text{--}25\text{ km}^2$  and temporal resolutions of 1–60 minutes. The umbrella cloud morphology is evaluated using digital image processing tools in a Lagrangian frame of reference. At the onset of neutral buoyancy, the radial spreading is better explained by a stronger dependence on time of  $r \sim t$ , rather than  $t^{2/3}$ ,  $t^{3/4}$ , or  $t^{2/9}$ . This flow regime exists on the order of minutes and has not been observed previously in satellite data. This may be of significance as it provides a means to rapidly (within the first 2–3 observations) determine the volumetric eruption rate. A hyperbolic tangent model,  $r \sim \tanh(t)$  is presented that matches the entire radial spreading time history and has a conserved torus-shaped volume in which the intrusion depth is proportional to  $\text{sech}(t)$ . This model also predicts the observed radial velocities. The data and the model estimates of the volumetric flow rate for the 15 January 2022 Hunga eruption are found to be  $3.6\text{--}5 \times 10^{11}\text{ m}^3\text{ s}^{-1}$ , the largest ever measured.

## RÉSUMÉ

Les panaches volcaniques forment des nuages en forme d'ombrelle dont l'évolution du rayon ( $r$ ) dans le temps ( $t$ ) a été précédemment modélisée par la théorie des courants de gravité, suivant asymptotiquement une loi  $r \sim t^f$  ( $f < 1$ ). Cependant, cette loi ne permet pas d'expliquer les observations satellite infrarouge d'ombrelles volcaniques. Nous caractérisons 13 nuages volcaniques en utilisant des données satellitaires avec une résolution spatiale de  $4\text{--}25\text{ km}^2$ , et une résolution temporelle de 1–60 minutes. La morphologie des ombrelles est caractérisée en analysant les images satellites dans un référentiel de mouvement lagrangien. Lorsque le panache arrête sa montée, l'extension radiale est mieux expliquée par un modèle linéaire  $r \sim t$ , plutôt que  $t^{2/3}$ ,  $t^{3/4}$ , ou  $t^{2/9}$ . Ce régime d'écoulement persiste pour une durée de l'ordre de la minute et n'a pas été observé par satellite précédemment. Il pourrait permettre d'estimer rapidement, en utilisant seulement les premières 2–3 observations satellites, le flux volumétrique de l'ombrelle. Nous proposons un modèle tangente hyperbolique pour l'extension radiale,  $r \sim \tanh(t)$ , qui permet de capturer l'évolution complète de l'ombrelle ainsi que de prédire la vitesse d'écoulement radiale. Le modèle suppose que le nuage conserve une forme de torus et que son épaisseur est proportionnelle à  $\text{sech}(t)$ . En utilisant ce modèle, nous estimons que le flux volumétrique de l'éruption Hunga en janvier 2022 est de  $3.6\text{--}5 \times 10^{11}\text{ m}^3\text{ s}^{-1}$ , le plus grand flux mesuré à ce jour.

KEYWORDS: Umbrella; Eruption; Flux; Infrared; Satellites; Volcano.

## 1 INTRODUCTION

Large, vertically extended eruption columns often form cloud structures that appear to have a 'mushroom' or 'umbrella' shape as they penetrate high into the atmosphere. From the perspective of a satellite, observing at close to a vertical viewing angle downwards, the umbrella appears to spread radially with time, often in an almost circular shape. The rate of spread in the radial direction (the radial spread or radial velocity) is related to the volumetric flow rate or volume flux ( $Q$ ,  $\text{m}^3\text{ s}^{-1}$ ) of material input to the atmosphere. This can be converted into a mass eruption rate (MER), and is important for estimating the impact of the emissions on the environment. Modellers have long grappled with the problem

of assigning a MER to describe the source conditions for an eruption, so that reliable forecasts of the amount and location of the emissions can be made [Mastin et al. 2009].

To understand the formation and propagation of umbrella clouds, researchers have modelled them as an intrusion; that is, a horizontal gravity current travelling into another stratified fluid, usually assumed to occur at the neutral buoyancy level [Benjamin 1968; Didden and Maxworthy 1982; Simpson 1999; Huppert 2006]. Gravity current intrusions have been studied in numerous fluid mechanics sub-disciplines [Chassignet et al. 2012, and references therein], including specifically, in the atmosphere [Flynn and Sutherland 2004; Costa et al. 2013; Johnson et al. 2015], in the ocean [Gill 1981], in rivers and coastal

\*✉ fred@aires.space

waters [Fischer et al. 1979], and in the laboratory [Lombardi et al. 2015]. Mathematical treatments of the problem in relation to volcanological umbrella clouds use the shallow-water approximation to numerically solve the Navier-Stokes equation [Ungarish and Zemach 2007; Johnson et al. 2015] and seek both self-similar solutions [George 1989] and non self-similar solutions to derive approximate asymptotic forms [Bursik et al. 1992; Costa et al. 2013; Johnson et al. 2015]. These asymptotic forms reveal power law relationships between the radial spread with time ( $t$ ) and distance ( $r$ ) [Johnson et al. 2015] and they have been generally found to agree with observations [Pouget et al. 2013; Pouget et al. 2016; Van Eaton et al. 2016; Hargie et al. 2019; Bear-Crozier et al. 2020]. Self-similar (scaling) arguments result in a power law exponent smaller than that found from numerical solutions of the shallow-water equations ( $t^{2/3}$  rather than  $t^{3/4}$ ); in other words, at least at the start of the flow, a stronger time-dependence of the radial spreading of the intrusive current's leading edge is found [Johnson et al. 2015]. In this study we seek to use parametrisations (e.g. power laws) that fit the observations to determine the volumetric flux as rapidly as possible so that they can be usefully used in dispersion models that attempt to forecast the movement and impact of volcanic emissions on the environment. Numerical solutions of the shallow-water equations are not investigated.

Recent studies have used satellite measurements to describe the evolution of the umbrella cloud and relate this to the MER [Pouget et al. 2013; Pouget et al. 2016; Van Eaton et al. 2016; Hargie et al. 2019; Bear-Crozier et al. 2020; Gupta et al. 2022; Jarvis et al. 2024]. Most of these studies use *ad hoc* methods for estimating the cloud area as a function of time and then utilise well-established theoretical models of gravity induced intrusion currents [Sparks et al. 1986; Woods 1988; Woods and Kienle 1994; Sparks et al. 1997] to relate the cloud volume flux to the MER. Under the assumptions of mass continuity, steady-state, and linear dynamics, the models variously predict volumetric changes proportional to  $t^f$ , where  $t$  is time and  $f$  is a fractional power, obtained through dimensional analysis and scaling arguments. Many of these papers determine a single MER by fitting data using time dependencies appropriate for the buoyancy-inertia driven regime, and the later dissipating regime of the intrusions' life-cycle. However, it is apparent that these relations break down at the initial stage of radial spreading where they predict impossibly large radial velocities. Rooney and Devenish [2014] show that at the start of the radial spread the radial velocity should be constant up to times  $t < \sim 3/N_f$ , where  $N_f$  is the Brunt-Väisälä frequency. Until now, this early part of the umbrella development has not been investigated using satellite observations.

The adequacy of the current approach to intrusive current flow has hardly been questioned despite the high disparity in estimates of  $Q$  (and subsequently the MER) and model underperformance in predicting the mass of erupted material [Aubry et al. 2023]. In only a few cases are the assumptions of steady-state and mass continuity justified, and especially at the onset of an eruption, when the complex and nonlinear nature of the generation of the intrusion suggests that a better description is needed. In this analysis, the generation of the

radially spreading intrusive current uses a new parametrisation that attempts to model the radial spread using a single function with multiple terms. The vertical flow of momentum produced by an erupting column is converted, usually at or near the tropopause (or once the neutral buoyancy height is reached), into a horizontal (radial) component that accelerates the intrusion from a very small radial velocity  $v_r$  to a constant radial velocity before decelerating at various rates before dissipation [Carey and Bursik 2015; Pouget et al. 2016]. The horizontal flow is principally driven by the initial upward vertical flux. The deceleration is due to loss of momentum caused by air resistance and for particle-rich plumes by sedimentation [Sparks et al. 1991; Ernst et al. 1996]. The lateral distance of its eventual dissipation depends on the MER and environmental winds [Carey and Bursik 2015]. At the start of the spread, because of the stratification of the atmosphere, vertical oscillatory behaviour is induced on time-scales of several minutes that can cause disturbances (waves) in the horizontal flow. These oscillations may play a role in the subsequent radial flow, and time series of the observed minimum cloud-top temperatures support the notion of damped, wave-like structures, previously noticed in a 3D numerical model of a spreading umbrella cloud [Suzuki and Koyaguchi 2009]. This aspect of the flow will be explored in greater detail in future work; here we hypothesise that the height of the leading edge of the spreading umbrella cloud may have a complicated time-dependent behaviour and resemble a localised wave-packet. Ungarish and Zemach [2007] used an instantaneous injection of an axisymmetric intrusion and found solutions of the shallow-water equations suggesting an expanding 'ring' structure with clear ambient air in the interior and thickening at the leading edge. A similar thickened leading edge was found by Johnson et al. [2015] in their shallow-water model solutions for a continuous axisymmetric intrusion. Building on these ideas, a new model for the radial velocity as a function of time is proposed in which the volume conserved is torus-shaped and the height of the leading edge (height of the intrusion) takes the form of a solitary wave packet. It is shown that this new model fits the observations of radial spread as well as models with  $\sim t^f$  ( $f < 1$ ) dependence. The new model also fits the time dependence of the radial velocity, better than the power law  $\sim t^f$ .

The analyses presented here are intended to stimulate a re-appraisal of the models used to describe the generation of the intrusion. The observations presented in this study provide compelling evidence that better physics is required to simulate the radial spread in the first tens of minutes after formation of the umbrella cloud. The practical importance of understanding the evolution of the radius of umbrella clouds for large explosive eruptions has recently been explored by Constantinescu et al. [2021] and a call for improvements is argued by Aubry et al. [2023].

## 2 METHODS

This study uses infrared satellite imagery to infer spatial and temporal properties of large volcanic clouds generated during explosive volcanic activity. Volcanic eruptions vary in size and intensity [Mason et al. 2004], and here we are only concerned with the subset of violent eruptions characterised

by a column with a spreading umbrella cloud of large radius ( $r \sim 10$ s km) reaching the upper troposphere or higher. The particle- and gas-rich column and cloud consists of volcanic ash with a broad range of particle sizes varying from very fine (particle radii  $< 16 \mu\text{m}$ ) to cm size fragments (lapilli) and larger fragmented rocks. The eruption plume also contains gases (principally  $\text{H}_2\text{O}$ ,  $\text{CO}_2$ , and  $\text{SO}_2$ ) which contribute to the energetics and dynamics of the turbulent rising column and cloud. As the column rises through the atmosphere, water may be entrained from the environment, and liquid and/or ice clouds form, making the rising column dark and opaque to visible and infrared radiation. The eruption may last from tens of minutes to several hours or longer and can be punctuated by periods of quiescence followed by further violent eruptions that can be more energetic than before. In the absence of strong windshear, an umbrella cloud usually forms at the level of neutral buoyancy [Sparks et al. 1997; Carey and Bursik 2015] with an overshooting column above.

From the perspective of an imaging instrument on board an orbiting satellite, there is an appearance of an almost circular cloud which becomes clearly discernible in visible and infrared light during the day and to infrared (IR) light at night. The spatial structure of the eruption cloud can be determined using either visible or IR imagery, and here we choose to use IR imagery as these data are independent of sunlight and the large opacity of the umbrella cloud helps to enhance the leading edges of the cloud. IR imagery from geostationary instruments supply data over the same location at time intervals of 1 minute to 1 hour and spatial resolutions of  $\sim 4$  to  $25 \text{ km}^2$ , so data from these platforms are exploited. The data sets used in this study are described in Table 1.

## 2.1 Brightness temperatures

The analysis of the data used here consists of identifying eruption clouds, estimating their area from IR measurements (single band centred at either  $11$  or  $12 \mu\text{m}$  wavelengths depending on instrument), and determining the rate of change of the size of the cloud. The main parameter used in the analysis is the IR brightness temperature ( $\text{BT}_v$ ), which is related to the measurement signal through a linear calibration from digital counts (or voltage) to radiance and then through use of the Planck function evaluated at a central wavenumber,  $\nu$ . In volcanological applications, satellite-derived brightness temperatures were first used by Prata [1989] in the context of volcanic ash detection. In future reference to brightness temperature we drop the subscript  $\nu$ , and because the clouds are optically thick, it can be assumed that the BT is a good measure of the thermodynamic cloud-top temperature  $T$ ; thus we simply refer to the BT as  $T$ . The calibration and conversion to brightness temperatures is a standard procedure. The data providers routinely evaluate the performance of the instruments and their calibration [Tabata et al. 2019], and there do not appear to be any issues that would affect the analyses presented here.

## 2.2 The umbrella cloud

A conceptual drawing of an idealised umbrella cloud is shown in Figure 1. The cloud consists of a spatially uniform top with

a circular shape and distinct edge. The edge of the umbrella is surrounded by a propagating front where the material properties of the cloud may be different to the interior of the cloud. From the geometric centre of the cloud outwards to the edge, the thermal structure is very uniform—there is a dense overcast region, similar to that found in tropical cyclones. The edge of the cloud is a subjective term and here we attempt to provide a quantitative definition based on digital image processing methods and a measure of infrared transparency. Umbrella clouds rarely maintain their shape and structure for longer than a few hours, and their diameters seldom exceed  $200 \text{ km}$ , making them smaller than the smallest category of tropical cyclone\*. This also means that inertial forces can usually be ignored, although in very large eruptions ( $\text{VEI}^\dagger \geq 6$ ) the Coriolis force plays a role [Baines and Sparks 2005]. Umbrella cloud sizes studied here range from radii of  $5$ – $550 \text{ km}$ , with lifetimes of 30 minutes to  $> 12$  hours. Figure 2 shows thermal and visible imagery for an eruption of Mt Etna that produced an exemplar umbrella cloud. There is a distinct cloud edge, a central overcast area where the temperature field is highly uniform and a nearly circular structure. These features are common to many of the umbrella clouds studied here.

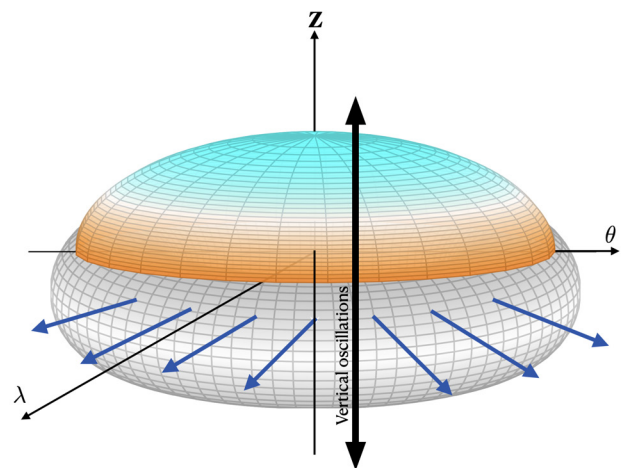


Figure 1: Conceptual depiction of umbrella cloud with protruding intrusion. The radial spreading  $r(t)$  and the radial velocity of the intrusion,  $dr/dt$  are both functions of time.  $Z$  is a vertical coordinate and  $\lambda$  and  $\theta$  are longitude and latitude, respectively. Vertical oscillations are generated which induce wave-like structures in the propagating intrusion.

## 2.3 Image processing

The goal of the analysis of the satellite  $T$  imagery is to estimate a radius,  $r$ , for the spreading umbrella cloud as a function of time. Satellite image data are obtained from various open access repositories (see the footnotes to Table 1 for sources) and the IR image data are converted to brightness temperature ( $T$ ) and re-projected from pixel/line to longitude/latitude ( $\lambda$ ,  $\theta$ )

\*This comparison with tropical cyclones is made only because of the similarity of cloud structure: similarity of dynamics and energetics is not being suggested.

<sup>†</sup>VEI is the Volcanic Explosivity Index [Newhall and Self 1982].

Table 1: Satellite data used in this study. The spatial scale denotes the nominal pixel resolution at the subsatellite point and increases with zenith viewing angle. The time given is the time of the first image used in the analysis (not the start of eruption). The links to data were valid at the time of writing this paper. In one case (Hunga) multiple geo satellites were able to view the eruption.

Volcano	Date (UTC)	Time*	Satellite	Location		Time sampling (mins)	Spatial sampling (km × km)	Source
				Lat °N	Lon °E			
Pinatubo	15.06.1991	05:41	GMS-4	15.13	120.35	60	5 × 5	[1]
Kelut	13.02.2014	16:32	MTSAT	-7.93	112.31	10–30	2 × 2	[2, 3]
Manam	31.07.2015	00:55	Himawari-8	-4.08	145.31	10	2 × 2	[4]
Calbuco	22.04.2015	21:37	GOES-13	-41.33	-72.62	30	2 × 2	[5]
Etna	04.12.2015	09:20	MSG-3	37.755	14.99	5	3 × 3	[6]
Tinakula	20.10.2017	19:23	Himawari-8	-10.38	165.80	10	2 × 2	[5]
Aoba	05.04.2018	13:57	Himawari-8	14.40	167.83	10	2 × 2	[5]
Krakatau	22.12.2018	13:56	Himawari-8	-6.10	105.42	10	2 × 2	[3, 4]
Raikoke	21.06.2019	18:11	Himawari-8	48.29	153.25	10	2 × 2 <sup>[8]</sup>	[5]
Ulawun	05.08.2019	04:55	Himawari-8	-5.05	151.33	10	2 × 2	[5]
Taal	12.01.2020	07:03	Himawari-8	14.01	121.00	10	2 × 2	[5]
Soufrière St Vincent	10.04.2021 <sup>[9]</sup>	09:47	GOES-16	13.33	-61.18	1	2 × 2	[7]
Hunga <sup>†</sup>	19.12.2021	20:47	Himawari-8	-20.54	-175.38	10	2 × 2	[5]
Hunga	13.01.2022	16:07	Himawari-8	-20.54	-175.38	10	2 × 2	[5]
Hunga	15.01.2022	04:17	Himawari-8	-20.54	-175.38	10	2 × 2	[5]
Hunga	15.01.2022	04:17/07:05	GOES-17	-20.54	-175.38	1	2 × 2	[7]

\* times are based on the first satellite observation, corrected for the scan-time dependence;

† Hunga (also called Hunga Tonga-Hunga Ha'apai);

[1] Holasek et al. [1996];

[2] Hargie et al. [2019];

[3] [https://www.data.jma.go.jp/mscweb/en/product/library\\_data.html](https://www.data.jma.go.jp/mscweb/en/product/library_data.html);

[4] Prata et al. [2020];

[5] <https://auth.diasjp.net/cas/login?service=http%3a%2f%2fhimawari.diasjp.net%2fexpert%2f>;

[6] <https://data.eumetsat.int/search>;

[7] <https://noaa-goes17.s3.amazonaws.com/index.html>;

[8] Resolution is lower at these latitudes; data are resampled to 2 × 2 km;

[9] Eruptions were detected from 10–12 April, 2021.

coordinates. The  $T$  image data can be used to calculate the following parameters, used here to define an umbrella cloud:

(1) The temperature gradient condition across a cloud edge can be estimated from

$$\left| \frac{dT}{d\rho} \right| > \gamma, \quad (1)$$

where  $T$  is the brightness temperature,  $\rho$  is a measure of distance in the image in the radial direction, and  $\gamma$  is a threshold temperature gradient. In practice the whole image is analysed using an edge detection algorithm. For example the Canny edge detector [Canny 1986], and the gradient of the image is computed using the Sobel-Feldman filter [Sobel and Feldman 1968; Gonzalez and Woods 2017], which is essentially a spatial derivative operator. (See Appendix A Figure A1 for an example). Equation 1 is then used only at the edge locations.

(2) We define the circularity  $C$  as:

$$C = \frac{4\pi A}{(\sum_i \ell_i)^2}, \quad (2)$$

where  $A$  is the area of the enclosing contour of a selected cold isotherm, and  $\ell_i$  is the arc length of consecutive points  $i$  on the perimeter of the contour. For a perfect circle  $C = 1$ . For elliptical shapes  $C$  depends on the eccentricity ( $e$ ): for  $e = 0.994$ ,  $C = 0.265$  and for  $e = 0.564$ ,  $C = 0.988$ . Initially circular umbrella clouds tend to deform towards elliptical shapes and become less convex with time. As the umbrella cloud develops, at some point in time it becomes detached from the source (moves away from the erupting vent location). From the perspective of thermal IR imagery it is not possible to determine vertical structure: detachment must be inferred from changes in the shape and position of the cloud, relative to its source.

(3) The roundness  $\mathcal{R}$  is defined as

$$\mathcal{R} = \frac{r_i}{r_c}, \quad (3)$$

where  $r_i$  and  $r_c$  are the radii of the inscribing and circumscribing circles (see Appendix A) of the selected isotherm, respectively.  $\mathcal{R}$  is an intuitive measure of the distortion of a shape from a perfect circle, but it does not provide information on the direction of distortion nor whether the shape is becoming less convex. Other measures of the shape of 2D objects are needed to assess distortion and these are calculated for each image using the Python *imea* library Kroell [2021]. See Appendix A for a discussion. More sophisticated shape measures and factors are described in Allen [2013] and the use of Fourier methods can be found in Schwarcz and Shane [1969]; these methods are not used nor required in this work but could be explored to investigate changes in cloud shape due to environmental factors. The distortion is related to background wind strength and direction, relative to the umbrella spreading, while the tendency to concavity and feathering is related to dilution and mixing effects [Basilio Hazas et al. 2023] at the edges of the intrusion, as well as loss of mass through particle sedimentation [Sparks et al. 1991]. These effects become dominant with time as the intrusion separates from its source and its velocity decreases.

(4) For all points inside the enclosing contour,

$$\bar{T}_c = \frac{1}{N} \sum_k^N T_k, \quad (4)$$

$$T_\sigma = \sqrt{\frac{1}{N-1} \sum_k^N (T_k - \bar{T}_c)^2} < \delta T, \quad (5)$$

where  $T_k$  corresponds to the  $T$  of pixels inside the contour,  $\bar{T}_c$  is the mean  $T$  of these pixels,  $T_\sigma$  the absolute value of the standard deviation of the  $T$  inside the contour,  $N$  is the total number of points inside the contour, and  $\delta T$  is a measure of temperature variability. The following values were used to define the umbrella clouds studied here:  $\bar{T}_c \leq 230$  K,  $\gamma = 5$  K km<sup>-1</sup>,  $\delta T = \pm 10$  K, and  $C \geq 0.4$ . The condition on  $C$  is relaxed for umbrella clouds in a strong background flow, which produce ‘cigar’-shaped umbrella clouds. While the values may seem arbitrary, they are based on analysis of 100s of images of circular-shaped high clouds.

Note that not all conditions must be met in order for the cloud to be classed as an umbrella cloud.

## 2.4 Contoured area equivalent radius—CAER

As the umbrella cloud does not always develop as a circular cloud, there is a need to define what is meant by an umbrella cloud radius. In this work we define this radius to be the radius of a circle which has the same area as an isotherm of the leading edge that encloses the spreading cloud, i.e. half the Heywood diameter [Heywood 1933]. This ‘equivalent’ radius is then used in the subsequent analysis to determine the radial spreading speed ( $v_r$ ) of the leading edge of the umbrella cloud.

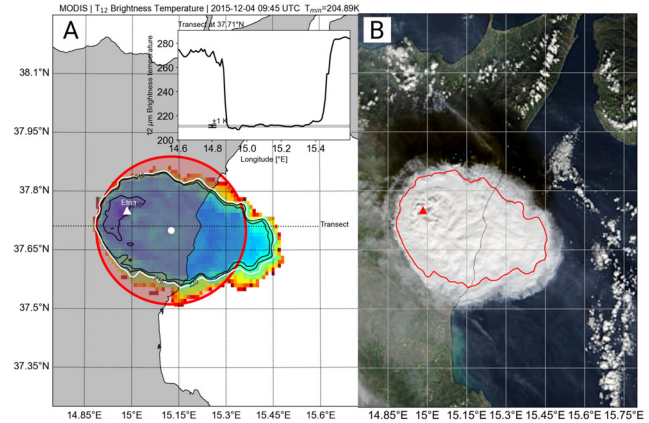


Figure 2: The umbrella cloud formed by an eruption of Mt Etna, Sicily on 4 December 2015 at 09:45 UTC. [A] MODIS/Terra 12  $\mu\text{m}$  brightness temperatures with an overlaid circle centred at the centroid of the cloud, and area equal to the area of the 220 K contour. The inset plot shows a transect across the 37.7° N latitude. Notice the very steep edge of the cloud and the uniform temperature field within the central overcast area. [B] MODIS/Terra true colour image of the same umbrella cloud with the same geographic projection. The true colour image is a good representation of what the cloud would look like to the human eye. The overcast area and sharp edge are clearly discernible. There is an indication of some circular undulations in the cloud field and the cloud has started to form an elliptical shape due to strong easterly winds at cloud level. The 220 K contour is also shown (red line).

Implicit in this analysis is that  $v_r$  is the same in all directions, which may be invalid in cases where there are strong directional winds. A more complex analysis can be undertaken by estimating the velocity components ( $v_\lambda$ ,  $v_\theta$ ) using, for example, optical flow techniques [Thomas and Prata 2018], and this will be explored in future work. The procedure for estimating the area of the cloud—the contoured area equivalent radius (CAER), is as follows:

- $T$  images corresponding to the first time the eruption is detected and up to when the cloud begins to dilute are reprojected onto a geographic map and contoured.

- The  $T$  contour corresponding to the edge of the umbrella is selected (using  $\left| \frac{dT}{d\rho} \right|$  at the edge locations) and its area calculated. The same contour is then used to calculate areas for all subsequent images up until the time conditions for the identification of an umbrella cloud are no longer met. The areas are computed using Green’s theorem as described in Prata et al. [2020] with a sufficiently dense set of coordinates, sampled in accordance with the spatial resolution of the raw data. Figure 3 illustrates the method for one image of the July 2015 Manam eruption.

- The location of the centroid of the selected closed contour is determined and the radius corresponding to a circle with the same area as the contour is calculated.\*
- The radial spread (or velocity,  $v_r$ ) as a function of time is then calculated using 1<sup>st</sup> order differences. Tracking the location of the centroid of the umbrella cloud in a Lagrangian frame of reference removes the effects of background winds on the calculation of  $v_r$ .
- Plots of  $r$  and  $v_r$  against time are constructed and functional fits established based on current theory and two new models (see later for details).

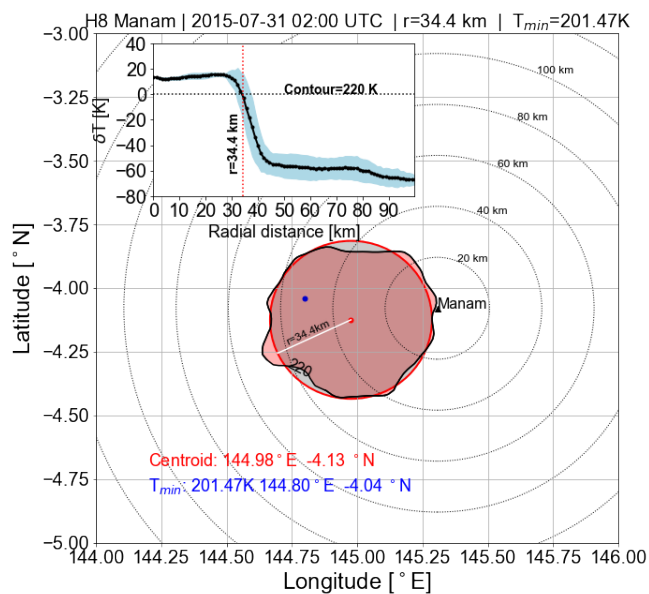


Figure 3: Estimating the enclosing contour of the leading edge of the umbrella cloud from thermal IR imagery. The area enclosed by the 220 K contour is shaded in red, while the area of the circle of radius  $r$  ( $r = 34.4$  km in this example) located at the centroid of the enclosing contour and which has the same area as the enclosing contour, is shaded in grey. The inset plot shows the temperature difference between the temperature of the enclosing contour (220 K in this example) and the mean of image pixels on the perimeter of circles of increasing radius from the centroid of the enclosing contour. The blue-coloured shaded region represents the azimuthal variability. The centroid of the umbrella cloud surface is no longer collocated with the location of the volcano and the minimum cloud temperature ( $\sim 201.5$  K) is neither over the volcano nor collocated with the centroid.

### 3 DATA

All of the data used are publicly available from open access archives maintained by national and international space agencies. Table 1 lists the data used, their sources, and characteristics for each volcanic eruption of relevance to this study. In addition, the data used to construct the radius and velocity versus

\*The area is calculated assuming a curved radius ( $r$ ) on a spherical earth (radius  $R_e$ ); for all cases  $r/R_e < 0.05$ .

time plots are included in an Excel file. In the eruptions studied, some generate small (radii  $< 50$  km) short duration ( $t < 60$  mins) umbrella clouds, whilst others have medium to large umbrella clouds (radii  $> 100$  km), last for several hours and may be punctuated by later discrete eruptions that influence the radial spreading. In a few cases, the horizontal winds have significantly distorted the shape of the propagating intrusion (from circular to ‘cigar’ shaped), and in one case (Krakatau) the intrusion is being continuously fed from below [Prata et al. 2020].

The locations of all of the volcanoes used in this study are shown in Figure 4.

### 4 MODELS OF RADIAL SPREADING

The umbrella (see Figure 1) has a skirt or ring-shaped leading edge of material that is spreading outwards from some central source point at a radial spreading speed of  $v_r$ . This speed changes with time (and distance) and is moderated by the source strength (i.e. mass eruption rate), gravity, viscous effects, turbulent mixing, and background winds. The isotherm used to evaluate the areal extent of the umbrella is assumed to remain at a constant height ( $z$ ), and the isotherm periphery as determined using the CAER procedure is taken as the physical outer boundary of the umbrella cloud.

Previous studies [Bursik et al. 1992; Johnson et al. 2015; Pouget et al. 2016] have determined the change in radius as a function of time asymptotically and fitted power-law relations of the form  $r \sim t^f$ , where  $f$  is some power. This implies that  $v_r \sim \frac{1}{f} t^{f-1}$ . The plots are reasonable, often because logarithmic axes are used, but closer inspection reveals that a multitude of functional forms can fit the measurements equally well. Inspection of Figure 8 of Sparks et al. [1986] which shows data points of  $v_r$  versus  $r$ , suggests that the  $r^{-1}$  functional form is not an especially good fit and there is an indication that at small cloud radii the measured  $v_r$  is lower than the theory suggests. In any case, in all of the data presented here,  $v_r$  is either increasing or relatively constant shortly after the intrusion starts to radially propagate. The generation of the intrusion is thought to be either driven by a continuous flow of mass from below at a steady rate, or a thermally driven fixed mass of material is emplaced at its neutral buoyancy height and then radial spreading occurs. In both circumstances the atmosphere must be stratified and the flow is maintained by a density difference between the upper and lower layers of the intrusion. The radial spreading will eventually stop, because the steady flow of mass stops and/or because atmospheric drag, mixing, and dilution (decreasing stratification) reduce the momentum.

Pouget et al. [2016] identify four time periods (regimes) where the driving force is either from buoyancy-inertia or turbulent drag and the cloud is either being fed with a constant flux of material or the volume of the intrusion is constant. Each of the regimes is characterised by a different power law, where the exponent decreases with time. In all cases the flow regimes are studied as long-time behaviours— asymptotes, guided by mathematical modelling [Johnson et al. 2015], i.e. some time after the umbrella cloud has formed; the order of this time-scale is  $\gg 3/N_f$ , where  $N_f$  is the Brunt-Väisälä frequency (see Table 2 for values of  $N_f$ ). Immediately

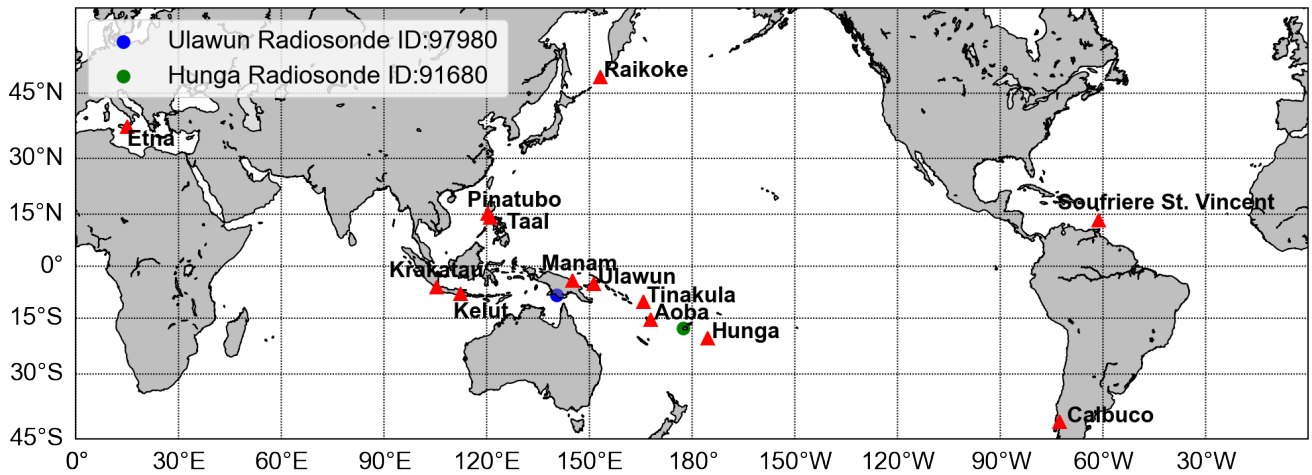


Figure 4: The locations of the volcanoes used in this study. The majority of volcanoes are within  $\pm 30^\circ$  of the equator and 9 of the 13 volcanoes are located in south-east Asia and the South Pacific. Raikoke is the furthest north volcano and Calbuco the furthest south. The locations of the two radiosonde stations cited in the text are shown as coloured closed circles.

after the umbrella cloud forms, the radial spreading is dominated by the momentum of the vertical collapse of the material due to the reduced gravity ( $g'$ ):

$$g' = \frac{N_f^2 h}{2}, \quad (6)$$

where  $h$  is the depth of the intrusion which may vary in time and space. Note also that  $N_f$  has a vertical dependence. The driving force in this case is the inertial upward pressure force of the erupting column, balanced by the rate of change of the radial kinematic momentum. In a descriptive sense, the volume of material that is forced upwards reaches a point of neutral buoyancy, overshoots and then collapses, but is prevented from falling further because of the upward pressure on its lower surface. The compression due to the pressure forces on the upper and lower surfaces stops the vertical motion of the material, and the radial pressure difference between the material inside and outside the intrusion drives it radially outwards. An assumption used in many models of volcanically generated atmospheric intrusive currents—also often referred to as gravity currents—is that the mass of the current is conserved (i.e. loss of mass by sedimentation of particles has been neglected) and that the source is steady. According to Woods and Kienle [1994], Sparks et al. [1997], and Costa et al. [2012, 2013] among others, a relation between the intrusion radius and time can be derived assuming it behaves as a gravity current:

$$r(t) = \left( \frac{3\lambda_{cs} N_f Q}{2\pi} \right)^{1/3} t^{2/3}, \quad (7)$$

where  $r$  [m] is radius,  $t$  [s] is time,  $N_f$  [ $s^{-1}$ ] is the Brunt-Väisälä frequency,  $Q$  [ $m^3 s^{-1}$ ] the volumetric flow rate and  $\lambda_{cs}$  is an empirical constant (a Froude number, sometimes referred to as the cloud shape parameter). The model described by Equation 7 is referred to here as the  $t^{2/3}$  model.  $Q_{2/3}$  is used to denote the volumetric flux estimated from the  $t^{2/3}$  model and in the more general context  $Q$  is used to denote volumetric

flux.  $Q_{2/3}$  can be estimated from this expression by estimating the coefficient  $B$  from a plot of  $r$  versus  $t^{2/3}$ :

$$B = \left( \frac{3\lambda_{cs} N_f Q_{2/3}}{2\pi} \right)^{1/3}. \quad (8)$$

Differentiating Equation 7, assuming no time dependence for  $N_f$  and  $Q_{2/3}$ ,

$$v_r(t) = \frac{2}{3} B t^{-1/3}. \quad (9)$$

The veracity of this formulation is tested by seeking fits to the measurements of  $r$  and  $v_r$  for the eruption umbrella clouds presented. Other time dependences of the radial spread have been suggested and shown to be more appropriate as the cloud develops and different physical processes become dominant, for example  $r \sim t^{3/4}$  [Bursik et al. 1992; Johnson et al. 2015; Pouget et al. 2016]. Ideally a single model parametrisation that incorporates all of the processes from the initial spreading through to dissipation is desirable.

If the goal is to determine the volumetric flux ( $Q$ ) from an eruption as quickly as possible so that a numerical model can be used to predict the amount of spreading material, then the assumption of constant radial velocity can be made. At the start of the formation of the umbrella cloud, the radial velocity is expected to reach a constant and can be determined from [Rooney and Devenish 2014]:

$$v_r = \frac{Q_c}{2\pi h_0 r_0}, \quad (10)$$

where  $r_0$  and  $h_0$  are the starting radius and intrusion depth, respectively.  $Q_c$  is subscripted to indicate that this is the value of  $Q$  determined from the constant velocity assumption at the start of the umbrella spreading. Thus if  $v_r$ ,  $r_0$ , and  $h_0$  are known or measured then  $Q_c$  can be estimated. This parametrisation is also investigated and referred to as the *constant velocity model*.

A new model (the *torus model*) is introduced here, based on theoretical reasoning assuming that the umbrella cloud maintains the shape of a torus. While this is clearly an idealisation

of the shape of the umbrella cloud, it is no less appealing than previous models that assume the cloud conserves its volume in the shape of a cylinder [Sparks et al. 1997]. This new formulation is introduced in Appendix B and provides an equation for the velocity as a function of time. This can be integrated analytically to give the radial spread as a function of time,

$$r(t) = \frac{2Q_t}{\pi^2 h_0^2 \alpha} \cosh^2(\omega t) [1 - \exp(-\alpha t)], \quad (11)$$

where  $\omega$  and  $\alpha$  are inverse time-constants,  $h_0$  the initial intrusion depth, and  $Q_t$  is the volume flux ( $Q$  determined from this model). These new parameters can be obtained using an optimised fitting procedure to data. Equation 11 is analytic and its time derivative gives the radial spreading velocity,  $dr/dt = v_r$  (see Appendix B). This model is referred to hereafter as the *torus* model and is also tested against the umbrella cloud measurements.

With the aim of finding a single expression that could model the complete time history of the radial spread and also be consistent with the radial velocity behaviour, another model is proposed that has three separate terms: a term involving the initial umbrella radius ( $r_0$ ), a term that includes the final velocity of the radial spread ( $v_f$  at time  $t_f$ ), and a term that captures the nonlinear time dependence ( $t$ ) at the start of the spread. This empirical model has the form

$$r(t) = a_0 \tanh(\omega_h t) + v_f t + r_0, \quad (12)$$

where  $a_0$  is a coefficient (units m or km) to be determined and  $\omega_h$  (units  $s^{-1}$ ) is an inverse time constant, not necessarily the same as  $\omega$  in the torus model. It follows from differentiation of Equation 12 with respect to time, that

$$v_r(t) = a_0 \omega_h \operatorname{sech}^2(\omega_h t) + v_f. \quad (13)$$

This is valid for  $0 < t < t_f$ , where  $t_f$  is the time at which the brightness temperature of the intrusion edge is indistinguishable from the background temperature. This model is referred to as the *hyperbolic* model and its form is influenced by requiring that it provides values consistent with observations at the start and end of the spreading. At  $t = 0$ ,  $r(0) = r_0$ ,  $v_r = \omega_h a_0 + v_f$ , and as  $t \rightarrow \infty$ ,  $v_r \rightarrow v_f$ . In order to estimate the volume flux,  $Q_h$  from this expression, it is assumed that at  $t=0$ ,  $Q_h \approx 2\pi h_0 r_0 \omega_h a_0$ . Making the approximation exact implies

$$a_0 = \frac{Q_h}{2\pi h_0 r_0 \omega_h}. \quad (14)$$

In the results to be presented the models are fitted to the measurements of radius as a function of time which determine the model coefficients. For the constant velocity, torus, and hyperbolic models  $h_0$  must be specified if  $Q$  is to be determined from the fits. The radial velocity and its variation with time provides an extra constraint since  $v_0$  and  $v_f$  can be calculated from the measurements. The calculation of  $Q$  from Equation 7 ( $Q_{2/3}$ ), Equation 10 ( $Q_c$ ), Equation 11 ( $Q_t$ ), and Equation 14 ( $Q_h$ ) for all of the volcano cases is provided in an Excel file, which also includes the coefficients of the fits for all four models.

## 5 RESULTS

For each of the volcanic eruptions (sometimes more than one for a particular volcano), the radial spread ( $r(t)$ ) of its umbrella cloud and the radial velocity ( $v_r(t)$ ) are calculated from the satellite thermal data, using the CAER procedure outlined previously. Model fits were performed so that volume fluxes could be estimated for the constant velocity ( $Q_c$ ),  $t^{2/3}$  ( $Q_{2/3}$ ), torus ( $Q_t$ ), and hyperbolic ( $Q_h$ ) models. The fitting was done using a trust region method (see Hofer et al. [2022] for details) from the `Scipy optimize curve_fit` package\*. The trust region reflective (trf) method with tight bounds was found to be generally robust and in addition provides error estimates on the optimised coefficients of the fit; however, for the torus and hyperbolic models, which involve several parameters, a different minimisation procedure was adopted (see Appendix C for further details). The radius measurement error ( $\sigma_r$ ) is assumed to be the same for each data point and equal to  $\sqrt{2} \times$  pixel size (km). The velocity measurement error is then  $2\sigma_r/\Delta t$ , where  $\Delta t$  is the time difference between successive measurements. For Himawari data, these errors are  $\pm 2.8$  km and  $\pm 1.1 \text{ ms}^{-1}$  for  $r$  and  $v_r$ , respectively. The accuracy of the fits can be judged by the mean bias (measured-model) and standard error for  $r$  and  $v_r$ .

Quantitative summaries of the performances of the models in relation to observations of the radius and velocity spreading as functions of time are shown in Figure 5 and Figure 6. Model performance is based on the statistics:

$$r_{bias} = \frac{1}{N} \sum_{i=1}^N |r_i - \hat{r}_i|; \quad (15)$$

$$r_{rmse} = \sqrt{\frac{\sum_{i=1}^N |r_i - \hat{r}_i|^2}{N}}; \quad (16)$$

$$v_{bias} = \frac{1}{N} \sum_{i=1}^N |v_i - \hat{v}_i|; \quad (17)$$

$$v_{rmse} = \sqrt{\frac{\sum_{i=1}^N |v_i - \hat{v}_i|^2}{N}}; \quad (18)$$

where  $N$  is the number of measurements,  $r_i$  is a radius measurement  $i$ ,  $\hat{r}_i$  is the model estimate,  $v_i$  is a velocity measurement and  $\hat{v}_i$  is the model estimate. Figure 5 shows the bias (observations – model) and standard deviation of the radial spreading for each eruption, for each model. In all cases, except for Calbuco-1, the bias lies within  $-6$  and  $+3$  km, and overall the bias for the three models is negative in the range  $-0.2$  to  $-3$  km. The overall standard deviation is largest where the umbrella radii are large, but within  $\pm 6$  km, with the torus and hyperbolic models having similar, and the lowest, bias and standard deviation. The Hunga results for the 15 January 2022 eruption have been omitted as multiple vertical layers of clouds have obscured the spreading umbrella cloud making it difficult to identify properly in the satellite data. It is also evident that none of the models perform particularly well (see

\*[https://docs.scipy.org/doc/scipy/reference/generated/scipy.optimize.least\\_squares.html](https://docs.scipy.org/doc/scipy/reference/generated/scipy.optimize.least_squares.html)

Table 2 for the values). Figure 6 shows the bias (observations – model) and standard deviation of the velocity spreading for each eruption, for each model. Whereas for the radial spreading it could be argued that the differences between the model results are not significant, this is not so for the velocity spreading. The torus and hyperbolic models biases are about half the size of the  $t^{2/3}$  model bias, and overall they all have a significant negative bias (model over-predicts observations). The standard deviation of the models are similar. The hyperbolic model outperforms the others largely due to the fact that it is able to reconstruct the radial spreading for longer. Most of the error in the model fits occurs at the later times, and the model fits for the three models at the start of the radial spreading are almost indistinguishable. For many of the eruptions, the model biases and standard deviations are small, but there are cases where none of the models perform well; for example Aoba and Calbuco-1.

Since the umbrella radii can be an order of magnitude different between eruptions, it is instructive to define a coefficient of variation for comparing models  $m$ ,  $m=1, 2$ , or 3. The coefficient of variation ( $C_m$ ) is a measure of the dispersion of the data relative to the mean, and allows comparisons between umbrella clouds of different size.  $C_m < 0.1$  is generally regarded as very good, whereas  $C_m > 0.3$  is poor.

$$C_m = \frac{\sigma_m(r)}{\mu_r}, \quad (19)$$

where

$$\sigma_m(r) = \sqrt{\frac{1}{N-1} \sum_{i=1}^N (r_i - \hat{r}_{m,i})^2}, \quad (20)$$

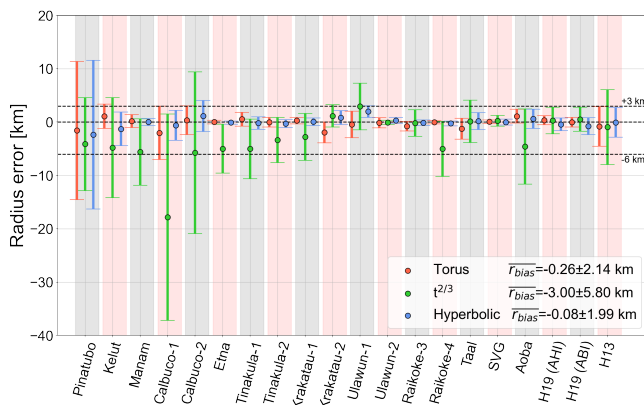


Figure 5: Biases ( $r_{bias} = \text{observations} - \text{model}$ ) and standard deviations for the radial spreading for all of the eruptions considered in this study, except for the 15 January 2022 Hunga eruption. Overall (all eruptions except Hunga 15 January 2022) biases and standard deviations are provided in the legend. H19 denotes 19 December 2021 eruption of Hunga; H13 denotes 13 January 2022 eruption of Hunga. ABI is the Advanced Baseline Imager and AHI is the Advanced Himawari Imager which are essentially the same instrument on board different geostationary platforms—GOES-17 and Himawari-8, respectively.

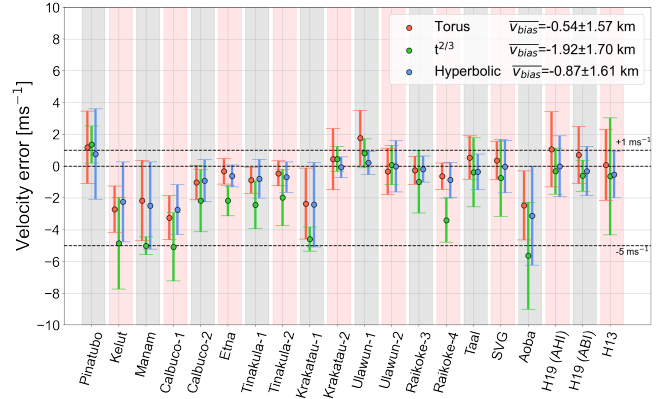


Figure 6: Biases ( $v_{bias} = \text{observations} - \text{model}$ ) and standard deviations for the velocity spreading for all of the eruptions considered in this study, except for the 15 January 2022 Hunga eruption. Overall biases and standard deviations (all eruptions except Hunga 15 January 2022) are provided in the legend. H19 denotes 19 December 2021 eruption of Hunga; H13 denotes 13 January 2022 eruption of Hunga. ABI is the Advanced Baseline Imager and AHI is the Advanced Himawari Imager which are essentially the same instrument on board different geostationary platforms—GOES-17 and Himawari-8, respectively.

and

$$\mu_r = \frac{1}{N} \sum_{i=1}^N r_i, \quad (21)$$

and  $N$  is the total number of data points for each case,  $r_i$  is the  $i$ th measurement and  $\hat{r}_{m,i}$  the  $i$ th model  $m$  estimate;  $\mu_r$  is the mean of the radius ( $r_i$ ) data, and  $\sigma_m(r)$  is the standard deviation of the measurement–model ( $m$ ).  $C_m$  is shown for all eruptions in Figure 7 where it can be seen that in all cases except two (Pinatubo and Ulawun-1) it is lower (more accurate) for the torus and hyperbolic models compared to the  $t^{2/3}$  model. This is due to the fact that the  $t^{2/3}$  dependence is not appropriate for modelling the later (decaying) stage of the umbrella radius spread. In the two exceptional cases, the umbrella intrusion has not reached the decaying stage. Much better fits for the  $t^{2/3}$  model can be obtained by only fitting the data for the emerging stage of the umbrella intrusion ( $n$  points) and  $C_{t^{2/3}}$  (black bars in Figure 7) is lower than, or the same as, for all points ( $N$ ) in 18 of the 21 cases, but still mostly larger than for the other models.  $C_{t^{2/3}}$  is not always lower because with  $n < N$ ,  $\mu_r$  is smaller, counteracting smaller  $\sigma_m(r)$  (e.g. Manam, Krakatau, and Aoba). Note that for optimal fits, the number of data points used for the models differs, as it became clear that two of the models could not fit the radial spread at later times. In the case of the constant velocity estimates, where  $v_r$  is estimated from the first few data points, and  $Q_c$  from Equation 10, the error arises from a combination of errors in estimating  $r_0$  and  $h_0$ . The total error on  $Q_c$  is estimated to be  $\pm 10\%$ . All of the results are summarised in Table 2 and provided in the Excel file.

Radius and radial velocity data and model fits are provided for all eruption cases in Figures 8 and 9, and can be viewed together with the table entries for each eruption. The plots are

drawn in exactly the same manner for ease of comparison. For the radius spreading the model fits all appear to be reasonable soon after the eruption (see Figure 8A–8U), but the  $t^{2/3}$  model is clearly inadequate for explaining the rate of change of the radius at later times (see Figure 9A–9U).

Since the eruptive history, environmental setting (e.g. atmospheric stability) and in some cases, the eruptive style, are different between eruptions, it is instructive to look in more detail. Two cases are discussed in the following subsections.

### 5.1 Umbrella cloud examples

Two eruptions are included for more detailed analyses: Ulawun and Hunga, as examples that help understand the overall results presented in Table 2 and in the statistical analyses of Figures 5, 6, and 7. The Ulawun eruption is presented first as this case exhibits many of the features expected for umbrella clouds, including rapid ascent, large circular shape, displacement from the location of the source vent (detachment), a secondary eruption and transport by the mean winds.

### 5.2 Ulawun

Mount Ulawun (5.050°S, 151.333°E, 2334 m asl) on the island of New Britain (see Figure 4) is a mixed basaltic/andesitic stratovolcano capable of small to quite large eruptions (VEI~1–4) [McKee et al. 2021]. The activity that started on 26 June 2019 culminated in a VEI~4 eruption at ~04:30 UTC and was imaged at 10 minute intervals by Himawari-8 with a first detection of an umbrella cloud at 04:50 UTC.\* At this time  $\bar{T}_c = 208.7$  K,  $\delta T_1 = 2.8$  K, and  $C = 0.954$ . At first detection, the equivalent radius<sup>†</sup> of the 220 K contour was 8.9 km. The Ulawun umbrella cloud was highly circular and remained so, even after the centroid of the cloud moved away from the volcano location. At 07:50 UTC, a small portion of the main contour became detached and consequently  $C$  decreased. Inspection of the images (Figure 10) suggests that between 06:00

and 06:10 UTC a second, larger eruption occurred causing an umbrella cloud that quickly merged with the first cloud.

After 07:10 UTC the two eruption clouds are indistinguishable; however the effect of the 2<sup>nd</sup> input is recorded as an acceleration in radial expansion, starting at 06:30 UTC. Table 2 shows the prescribed and estimated parameters for both Ulawun eruptions. More detailed analysis of this eruption is shown in Figure 11 for the  $t^{2/3}$  and the hyperbolic models to highlight the temporal behaviour. There is a noticeable change in  $v_r$  at ~06:30 UTC, and another later at ~08:00 UTC, although this is less clear and may also be due to detachment. The initial increase in  $v_r$  and change at 06:30 UTC can be associated with separate explosions and hence changes in the volume flux. Consequently these are modelled with different hyperbolic model coefficients. The  $t^{2/3}$  fit for the initial explosion gives an adequate fit to both the radius and velocity, except at the start of the umbrella expansion where this model suggests unrealistically high initial velocity (as  $t \rightarrow 0$ ,  $v_r \rightarrow \infty$ ). For the second eruption the velocity fit is quite poor throughout. By selecting coefficients for the hyperbolic model, consistent and accurate fits to the radial spread and the velocity time-dependence can be obtained, including the periods of acceleration of the radial expansion. However, could the change in  $v_r$  be due to the background winds? The effect of the background winds can be significant and in some cases the movement of the intrusion may be dominated by the winds at the level of neutral buoyancy. To investigate their significance for Ulawun, radiosonde profiles at Merauke (8.466°S, 140.333°E, ~1200 km SW of Ulawun; see map in Figure 4) for 00 and 12 UTC on 26 June 2019 were examined. The skew-T plot for 12 UTC (Supplementary Material 1 Figure S1) shows a tropopause at ~18 km with a temperature no lower than 190 K, suggesting that the umbrella cloud is close to or at the tropopause. The umbrella cloud is beginning to elongate in the NW–SE direction and by now there is no mass supply to the cloud—it is dissipating. The background winds in this case are not particularly strong (~10–20 m s<sup>-1</sup>) and are going from the west to towards the east between 15–18 km (see Supplementary Material 1 Figure S1). The methodology used to determine radial velocities follows the motion of the cloud by tracking the centroid of a selected isotherm and so the background winds do not affect their calculation. This Lagrangian approach ensures that the background winds are removed from the calculation of  $v_r$ . In order to check on the representativeness of the Merauke profile wind vectors, reanalysis data was examined at 250 hPa and 10 hPa and winds were found to be relatively uniform over the region.

The life-cycle of the Ulawun umbrella cloud intrusion can be described by an initial acceleration then a small period of constant velocity followed by a rapid deceleration. A second impulse of energy from another eruptive phase begins the cycle again. After a few hours, with diminished or no further eruptive activity the cloud is no longer being fed with material from below, its shape distorts and the cloud is dispersed by the background winds, or the cloud is no longer detectable because the cloud is too optically thin. This pattern of events appears to apply to some of the other clouds studied here, with each of the periods in the life-cycle differing in ampli-

\*This is the Sector start time of the Himawari image data. The actual time at the pixel depends on the Sector (there are ten) and pixel number within the Sector. For Ulawun the actual pixel time is ~5 min 30 s later than the Sector start time. As the actual time is not used quantitatively in this study, all times are referred to using the Sector start time.

<sup>†</sup>For brevity, in future reference to *radius* implies the *equivalent* radius.

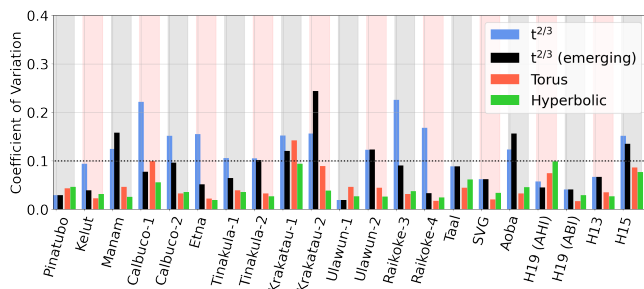


Figure 7: Coefficient of variation for radius fits for the three models for all of the eruption umbrella intrusion studied. The  $t^{2/3}$  model fitted with data only for the emerging stage ( $n \leq N$ ) of the spreading intrusion is shown as black bars.

Table 2: Umbrella cloud parameters relevant to the calculation of volumetric fluxes ( $Q$ ). The volumetric flux determined for each eruption is given for an assumed intrusion depth of  $h_0$ .  $Q_c$  corresponds to the flux calculated for constant velocity, using  $h_0$  and  $r_0$ , the initial radius of the umbrella cloud.  $Q_r$  corresponds to the flux calculated assuming a torus shaped intrusion.  $Q_{2/3}$  corresponds to the flux calculated assuming a  $r^{2/3}$  time dependence for the radial spread and  $Q_h$  corresponds to the flux for the hyperbolic model using Equation 14. The maximum radial velocity and final umbrella radius are also given.

Volcano	Height range (km)	Brunt-Väisälä $N_f$ ( $s^{-1}$ )	Radial velocity ( $m s^{-1}$ )	$r_0$ (km)	Max. radius (km)	Intrusion depth $h_0$ (km)	Volume flux ( $\times 10^9 m^3 s^{-1}$ )			
							$Q_c$	$Q_r$	$Q_{2/3}$	$Q_h$
Pinatubo	18–22	0.028	23.9	40.0	570.0	10.0±1.0	65.97±6.6	44.00±14.9	47.71±0.58	37.70
Kelut	18–21	0.030	26.7	16.0	141.0	4.0±0.4	10.72±1.1	8.64±0.43	10.33±0.1	9.73
Manam	18–20	0.026	23.0	4.7	45.7	2.5±0.3	1.71±0.2	2.84±0.33	2.53±0.1	1.42
Calbuco <sup>1</sup>	15–17	0.017	9.2	11.8	68.1	3.0±0.3	2.92±0.3	2.70±0.25	2.31±0.1	2.86
Calbuco <sup>2</sup>	15–17	0.017	12.8	10.1	112.7	3.0±0.3	2.14±0.2	2.54±0.01	2.51±0.1	2.19
Etna	10–14	0.017	9.1	5.4	27.9	1.5±0.2	0.47±0.4	0.51±0.01	0.37±0.1	0.45
Tinakula <sup>1</sup>	14–16	0.012	12.9	8.1	51.2	3.0±0.3	1.98±0.2	2.39±0.18	2.48±0.1	1.84
Tinakula <sup>2</sup>	14–16	0.012	12.9	8.1	51.2	3.0±0.3	1.98±0.2	2.48±0.50	1.71±0.1	1.71
Krakatau <sup>1</sup>	17–19	0.020	14.3	5.7	41.2	2.0±0.2	1.03±0.1	1.92±0.09	1.05±0.1	0.72
Krakatau <sup>2*</sup>	17–19	0.020	5.5	11.6	58.8	2.0±0.2	0.49±0.1	0.43±0.03	0.16±0.1	0.27
Ulaun <sup>1</sup>	16–18	0.024	10.5	5.7	~40	2.0±0.2	0.76±0.1	0.73±0.25	0.50±0.1	0.68
Ulaun <sup>2</sup>	16–18	0.024	9.8	8.9	74.6	2.0±0.2	1.06±0.1	1.00±0.33	0.45±0.1	1.04
Raikoke <sup>3</sup>	15–18	0.019	20.0	6.0	28.2	2.0±0.2	1.51±0.2	1.76±0.17	1.84±0.1	1.32
Raikoke <sup>4</sup>	15–18	0.019	9.7	6.8	23.3	2.0±0.2	1.71±0.2	1.44±0.08	0.86±0.1	1.20
Taal	17–21	0.031	12.1	9.3	124.4	2.5±0.3	1.76±0.2	1.94±0.12	2.01±0.1	1.46
SVG	16–18	0.020	22.8	6.3	25.2	2.0±0.2	1.82±0.2	1.81±0.04	1.37±0.1	1.29
Aoba	14–16	0.011	24.8	13.7	63.4	4.0±0.4	8.51±0.9	9.44±4.29	11.34±0.5	7.56
Hunga <sup>5</sup>	16–20	0.024	16.3	12.0	131.9	2.5±0.3	3.10±0.3	2.25±0.09	2.60±0.1	2.43
Hunga <sup>6</sup>	16–20	0.024	16.3	12.0	121.0	2.5±0.3	3.10±0.3	2.25±0.09	2.43±0.1	2.58
Hunga <sup>7</sup>	16–20	0.024	14.8	15.2	172.4	4.0±0.4	5.65±0.6	5.83±0.27	6.55±0.1	4.32
Hunga <sup>8,9</sup>	17–35	0.021	79.1	57.9	220.0	15.0±1.5	431.7±43.2	436.5±158.5	395.0±23.8	435.46

<sup>1</sup> 1st eruption;

<sup>2</sup> 2nd eruption;

<sup>2\*</sup> 2nd eruption Continuous phase starting at 17:34 UTC;

<sup>3</sup> Starting at 04:02 UTC 22.06.2019;

<sup>4</sup> Starting at 18:12 UTC 22.06.2019;

<sup>5</sup> Eruption on 19 December 2021–ABI (the Advanced Baseline Imager);

<sup>6</sup> Eruption on 13 January 2022–AHI (the Advanced Himawari Imager);

<sup>7</sup> Eruption on 15 January 2022–ABI;

<sup>8</sup> Eruption on 15 January 2022–AHI;

<sup>9</sup> The Brunt–Väisälä frequency is calculated using the closest in time, nearby radiosonde profile except in this case where it is estimated from the US Standard Tropical atmosphere. In all cases  $N_f$  is the mean over the height range shown (see also Figure S2, [Supplementary Material 1](#)).

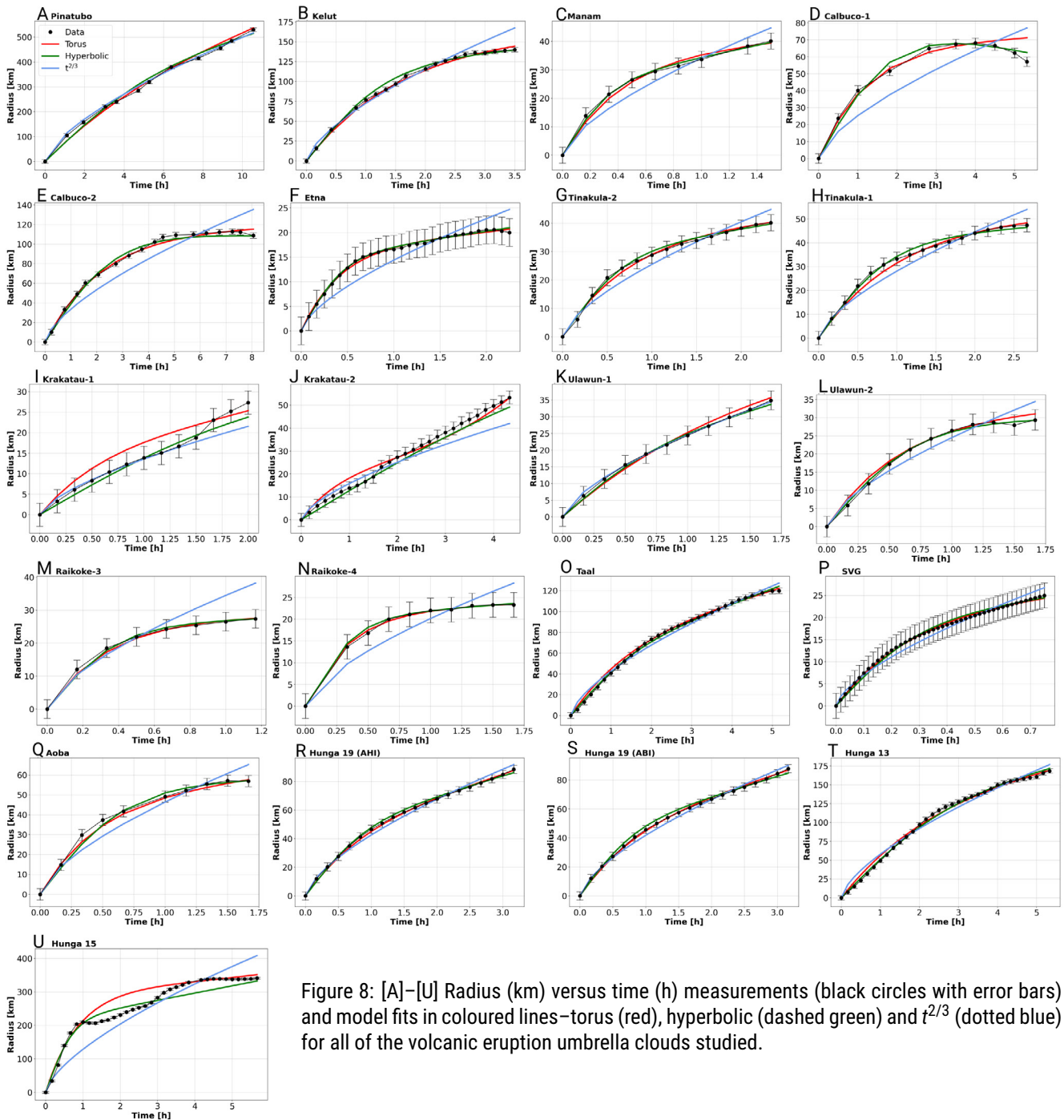


Figure 8: [A]–[U] Radius (km) versus time (h) measurements (black circles with error bars) and model fits in coloured lines–torus (red), hyperbolic (dashed green) and  $t^{2/3}$  (dotted blue) for all of the volcanic eruption umbrella clouds studied.

cation or diminution, number of eruptive phases, and in the significance of the background winds.

### 5.3 Hunga, 2021/2022

The Hunga volcano\* erupted violently on 19 December 2021 and on 13 January 2022 generating a large umbrella cloud and again, more violently on 15 January 2022 [Matoza et al. 2022]. The eruption chronology and insights from volcanic lightning data have been studied by Gupta et al. [2022], Jarvis

et al. [2024], and Van Eaton et al. [2023]. There were at least 3 large explosions on 15 January and each may have produced separate intrusions that became superposed and difficult to separate in the data. The eruption columns were very high [Carr et al. 2022], possibly reaching 57 km [Proud et al. 2022]. Data for the eruptions on 19 December and 13 and 15 January were obtained from Himawari-8 at 10 minute intervals and from the GOES-17 ABI also at 10 minute intervals and at 1 minute intervals for some periods of the eruptions on 15 January. These three eruption episodes are discussed separately.

\*The Hunga volcanic eruption is also referred to in the literature as the Hunga Tonga-Hunga Ha’apai eruption. The two islands Hunga Tonga and Hunga Ha’apai are the observable surface features of the submerged Hunga volcano.

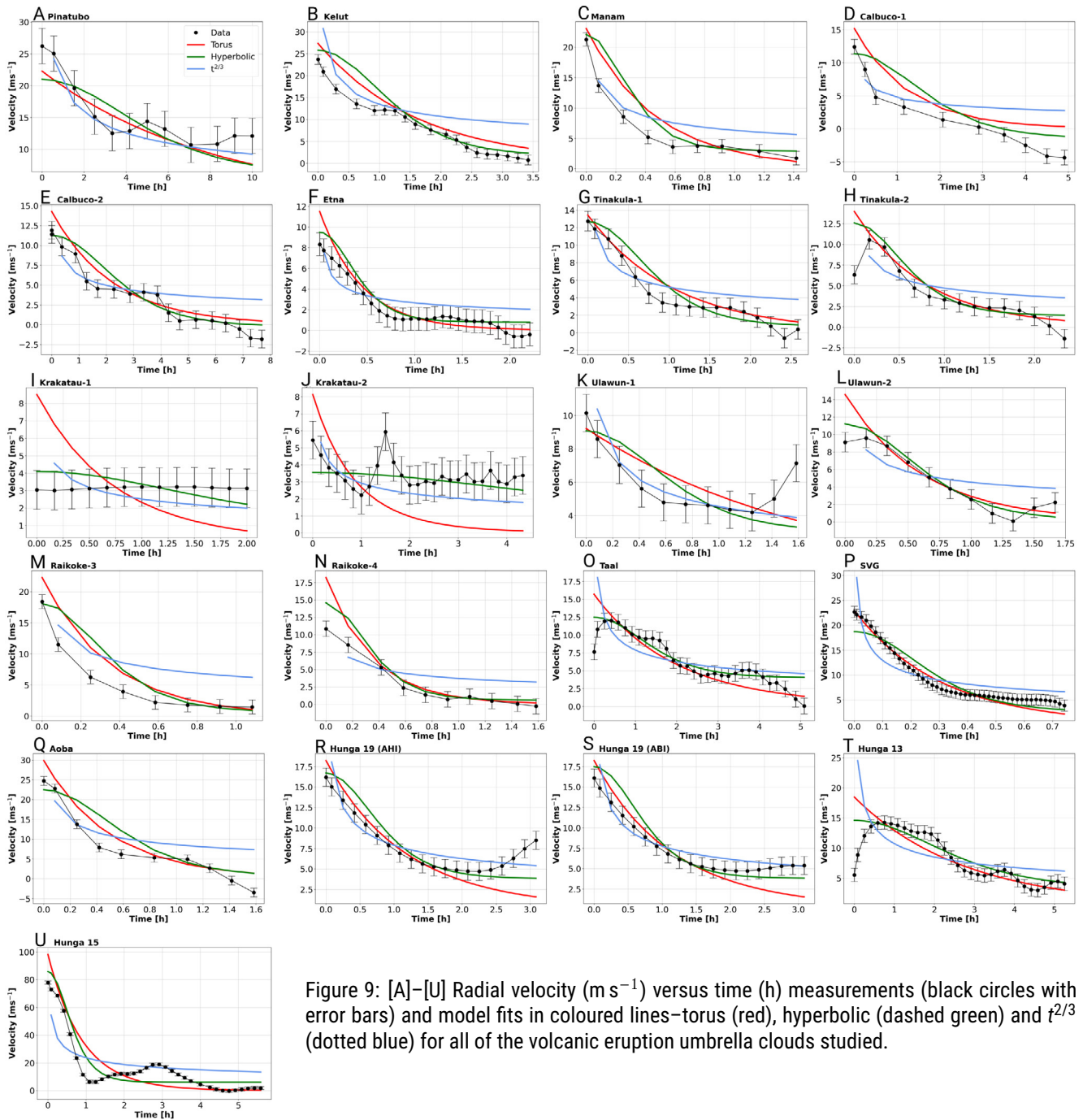


Figure 9: [A]–[U] Radial velocity ( $\text{m s}^{-1}$ ) versus time (h) measurements (black circles with error bars) and model fits in coloured lines—torus (red), hyperbolic (dashed green) and  $t^{2/3}$  (dotted blue) for all of the volcanic eruption umbrella clouds studied.

### 5.3.1 19 December 2021

The 19 December eruption was first noticed in Himawari-8 data at 20:40 UTC (20:47 UTC at the volcano) and it produced a large umbrella cloud (maximum radius  $\sim 130$  km) which lasted  $\sim 5$  hours. The analyses for the 19 December are shown in Figure 12. The umbrella cloud remained very circular ( $C > 0.85$ ) up to about 2 hours after the initial eruption and then became oval shaped, distorted in a SW–NE orientation. In this case both AHI and ABI data at 10-minute intervals were available and analysed separately. A single Sentinel-3 OCLI/SLSTR image was also acquired at 21:20 UTC on 19 December 2021. The degree of agreement between the radius estimates for all three sensors is very good. The fits using the

hyperbolic, torus and  $t^{2/3}$  models are all good and volumetric fluxes ( $Q_t$ ,  $Q_{2/3} = 2.25, 2.60 \times 10^9 \text{ m}^3 \text{ s}^{-1}$ ) estimated using the models are also in agreement (within 15%). The start of the eruption was estimated to be 20:35 UTC based on model fitting and agrees with the estimate reported by Carn et al. [2022]. The volumetric fluxes were estimated to be  $\sim 3.1$  and  $2.43 \times 10^9 \text{ m}^3 \text{ s}^{-1}$  for the constant velocity and hyperbolic fits. All of the parameters used in the fits are given in the Excel file.

### 5.3.2 13 January 2022

The eruption on 13 January which began at  $\sim 15:20$  UTC was large, with an umbrella cloud reaching and penetrating the

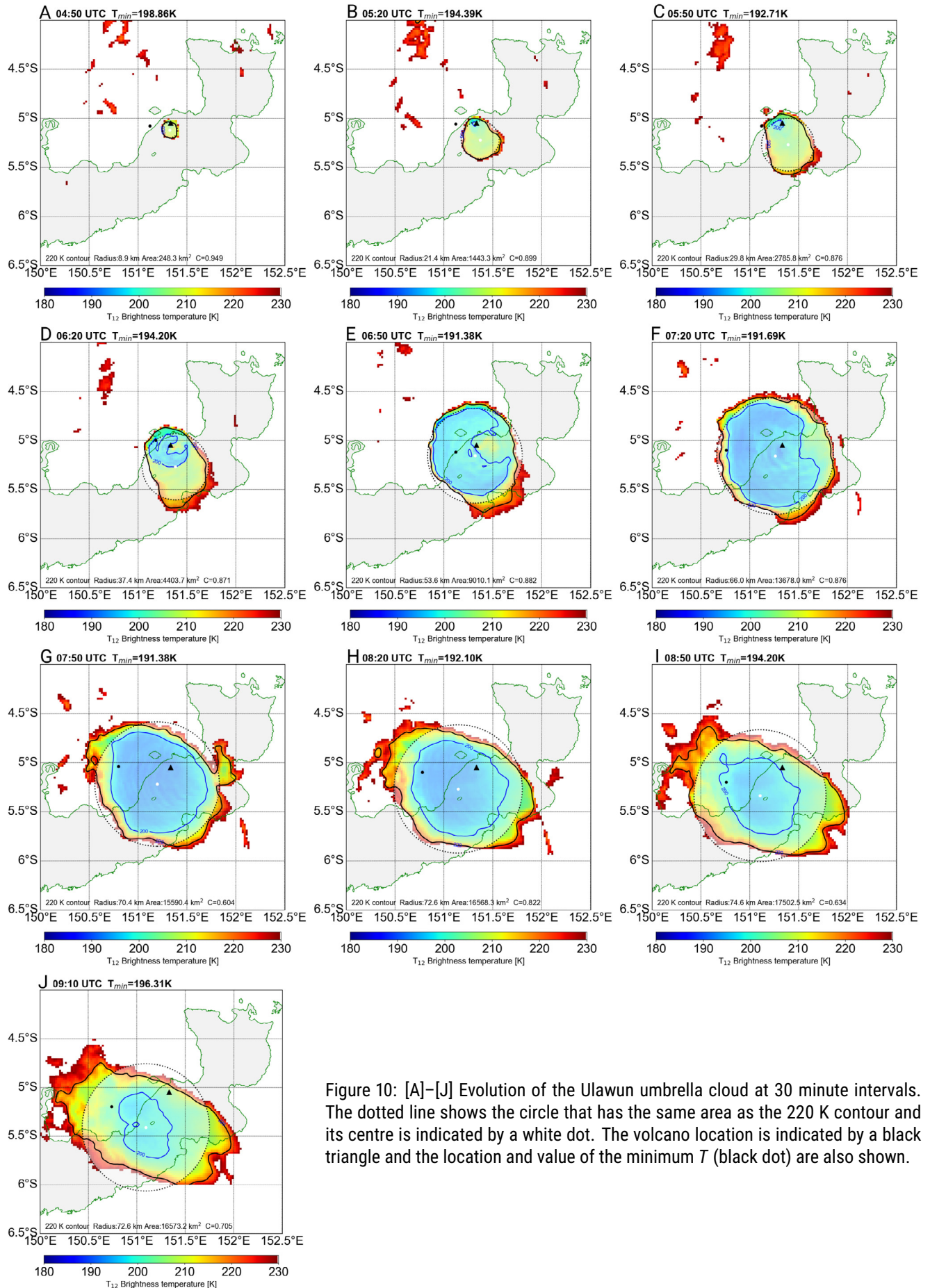


Figure 10: [A]–[J] Evolution of the Ulawun umbrella cloud at 30 minute intervals. The dotted line shows the circle that has the same area as the 220 K contour and its centre is indicated by a white dot. The volcano location is indicated by a black triangle and the location and value of the minimum  $T$  (black dot) are also shown.

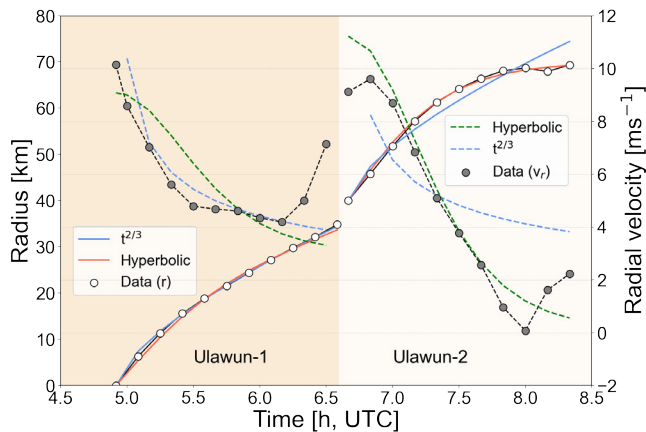


Figure 11: Radius and radial velocity ( $v_r$ ) as a function of time for the 26 June 2019 Ulawun eruption. Data points are indicated by coloured circles. Fits to radius versus time are shown by solid lines using the  $t^{2/3}$  mode and the hyperbolic model that includes a radius offset, a constant velocity term and a hyperbolic tangent dependence. The  $v_r$  versus time fits are shown as dashed lines, determined by differentiating the radius fits. The abscissa is time (in hours, UTC) and the ordinate is radius (in km, left-hand side, open circles) and velocity (in  $\text{m s}^{-1}$ , right-hand side, grey circles). Dashed (for velocity) and continuous (radius) lines are fits based on theoretical models. In both cases the velocity fits are determined by differentiation of the modelled radius fits.

tropopause. It was first detected in Himawari-8 data at 15:30 UTC and a minimum temperature of  $\sim 185$  K was recorded in the image of 16:10 UTC, by which time the umbrella cloud had formed at the neutral buoyancy level and radial spreading is evident. Figure S2 (Supplementary Material 1) shows vertical profiles of the temperature, humidity, Brunt-Väisälä frequency and air density on 13 January at 00 UTC obtained from a profile (Figure S3, Supplementary Material 1) at a nearby radiosonde station ( $\sim 700$  km, see Figure 4). There is a tropopause at around 18 km where the minimum temperature is 190 K Supplementary Material 1. Minimum temperatures in subsequent Himawari-8 images vary between 185–190 K, suggesting that the cloud was located near the tropopause. It is reasonable to assume that 10 minutes after the initial eruption the umbrella cloud had reached maximum height and had started to spread as a gravity-driven current (intrusion). Pouget et al. [2016] investigated flow regimes for the umbrella clouds of several large eruptions, including two of the case studies presented here (*viz.* Pinatubo and Kelut). They found that the initial spread was governed by time dependencies of  $\sim t^{2/3}$  and  $\sim t^{3/4}$  when they assert gravity was the driving force, while the latter stages of the spread followed  $\sim t^{2/9}$  and  $\sim t^{5/9}$ , when they assert turbulent drag dominates. The value of the exponent for the time dependence in the turbulent drag regime was largely determined by whether the eruption was short-lived or in continuous eruption. For the 13 January eruption the initial spreading ( $t \lesssim 17:10$  UTC) does not seem to follow  $\sim t^{2/3}$  particularly well, but  $\sim t^{3/4}$  appears to be better. The fits for  $v_r$  are poor for  $t^{-1/3}$  and  $t^{-1/4}$ .

The time dependence of the radial velocity is shown in Figure 13. By 15:40 UTC there is a very circular umbrella cloud, remaining circular for several hours, propagating with  $v_r$  increasing initially and then reaching  $\sim 15 \text{ m s}^{-1}$  which remains relatively constant for  $\sim 30$  minutes and thereafter decelerates to  $\sim 3 \text{ m s}^{-1}$  at the end of the observations (Figure 13). There is an indication of an increase in velocity at around 18:50 UTC, suggesting that there may have been a second large injection of energy into the cloud (*i.e.* a second large eruption); initial reports\* suggest a continuous eruption until  $\sim 21:30$  UTC. In this case and in others there appears to be a pattern of near constant or slowly decreasing  $v_r$  in the first tens of minutes after the umbrella cloud forms.

### 5.3.3 15 January 2022

At  $\sim 04:15 \pm 3$  minutes UTC on 15 January 2022 Hunga volcano generated the most energetic eruption in the last  $\sim 140$  years and was at least as energetic as Krakatau in 1883 [Matoza et al. 2022; Wright et al. 2022; Yuen et al. 2022]. Himawari-8 AHI and GOES-17 ABI 10-minute data were acquired for the duration of the paroxysm, while ABI 1-minute data were acquired from 07:05 UT, about 2.75 hours after the start of the eruption. The umbrella cloud with radius  $\sim 21$  km was first observed in Himawari-8 data in the 04:10 UTC segment, which corresponds to 04:17 UTC at the location of sensing at Hunga†. The cloud is opaque and the cloud-top temperatures have dropped below  $\sim 180$  K (Figure 14), suggesting that the umbrella had reached the tropopause (inset plot in Figure 14) and there is considerable undercooling occurring. The cloud continued to penetrate high into the stratosphere and inspection of the satellite data shows that radial spreading occurred at two different levels. The great height ( $\sim 57$  km [Proud et al. 2022]), multiple explosions and large radial extent make this eruption particularly difficult to analyse. It is likely that two separate intrusions were generated [Gupta et al. 2022]: one between 15–25 km and another above 32 km (see Figure 15). Since temperatures increase in the stratosphere, analysis of the upper intrusion is difficult when using brightness temperature isotherms as they become confused with tropospheric isotherms.

The complete time history of the umbrella radius and its radial velocity for the 15 January eruption is shown in Figure 14. The upper plot shows the radius change with time, while the lower plot shows the radial velocity change with time. None of the models shown fit the entire time history particularly well. The initial rapid spreading is slowed from  $\sim 05:20$  UTC, but increases again from just before 07:00 UTC. This can be seen more clearly in the velocity variation. In the first hour or so, there is rapid radial spread with an initial radial velocity of  $\sim 75 \text{ m s}^{-1}$ . Following this, the change is more gradual and then levels out beyond 08:00 UT. Van Eaton et al. [2023] find a plume at  $\sim 15$  km a.s.l. between 02:57–03:20 UTC (at the volcano location) using GOES-17 data, whereas there is no evidence of a plume in the Himawari-8 AHI data before 04:17 UTC on 15 January 2022 or in the GOES-17 thermal

\*<https://matangitonga.to/2022/01/15/tongan-geologists-stunning-Jan14eruptions>

†The ABI data give radii of 18, 18.8, and 20 km, for isotherms 235, 240 and 245 K, respectively.

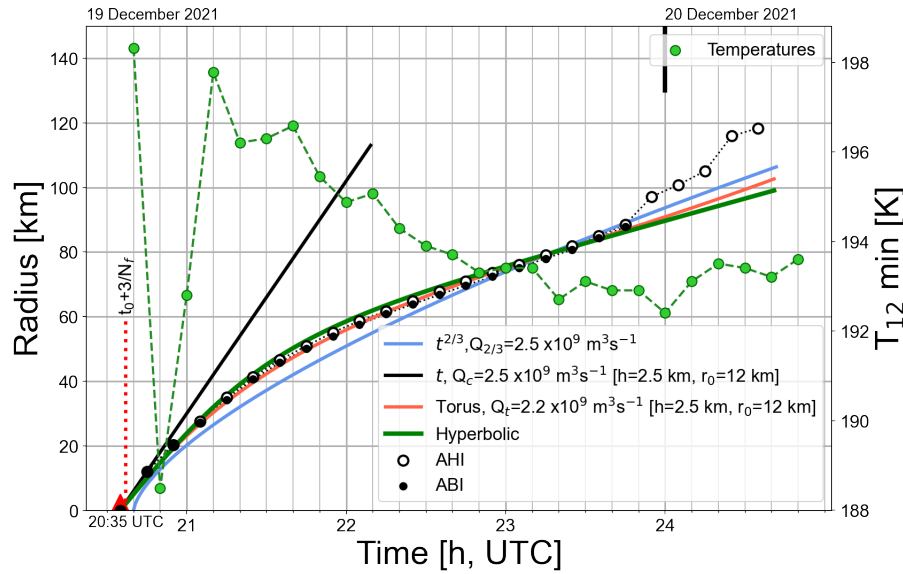


Figure 12: Radius as a function of time for the 19 December 2021 eruption of Hunga volcano determined from 10-minute AHI (open circles) and ABI data (closed circles). Fits based on  $t^{2/3}$ , hyperbolic, torus, and  $t$  (constant velocity) models are shown, along with estimates of the flux for three models. The parameters used and the flux estimates are also available in the Supplementary Excel file.  $t_0$  is the assumed start of the eruption,  $\approx 12$  min before the first observation. The AHI  $T_{12}$   $\mu\text{m}$  minimum cloud-top brightness temperature is shown in light-green (right-hand side ordinate) showing the rapid drop in temperature as the umbrella cloud reaches and penetrates the tropopause. The theoretical time limit expected for the constant velocity regime is indicated by a dotted red line. The red triangle on the abscissa marks the time of the eruption.

data used here. This is likely due to an error in their cloud shadow analyses, which does not affect their estimate of the MER of  $\sim 0.5\text{--}1 \times 10^{10} \text{ kg s}^{-1}$ , equivalent to volumetric flux range of  $3.2\text{--}5.5 \times 10^{11} \text{ m}^3 \text{ s}^{-1}$ . The analysis done here for the ABI data (not shown) gives  $Q_t = 4.1\text{--}5.2 \times 10^{11} \text{ m}^3 \text{ s}^{-1}$ .

Radius versus time fits using the constant velocity and  $t^{2/3}$  dependencies are both reasonable in the rapid spreading regime but poor afterwards. The time history (Figure 14) is best explained by three separate injections of material from eruptions at 04:15, 04:27, and 04:47 UT. Ichihara et al. [2023] report eruption times at 04:14, 04:51, 05:34, and 08:33 UTC which correspond well to two of the three eruption times found here, and the later ones at  $05:37 \pm 3$  minutes and  $08:31 \pm 3$  minutes (see Figure 14A). It is also interesting to note that Ichihara et al. [2023] describe observations of a second lightning ring around 05:09–05:29 UTC, which can be associated with an eruption at 04:47/04:51 UTC generating an intrusion with  $v_r \sim 74 \text{ m s}^{-1}$ .

The lower plot also shows the surface pressure trace from Tonga ( $\sim 70$  km from Hunga) with large pressure anomalies corresponding to the passage of explosive energy (in the form of fast travelling gravity waves). If we take the time difference between the time of no acceleration ( $d^2r/dt^2 = 0$ ) using the  $\tanh(\omega_h t)$  fits and the eruption times (based on the passage of the pressure waves), and calculate the great circle distance between Hunga volcano and the leading edge of the umbrella, then the implied initial radial velocities are  $\sim 78$ ,  $74$ , and  $69 \text{ m s}^{-1}$ , suggesting the volumetric fluxes from each eruption were very similar. Since these later eruptions are not directly detectable by the observations presented here, due to cloud

opacity, the implied initial velocities are greatly underestimated. The initial velocities found here agree (within 10–20%) with the estimate given by Ichihara et al. [2023] of  $64 \text{ m s}^{-1}$ . Assuming an intrusion depth of 15 km for the initial intrusion gives values for the model fluxes of  $Q_c = 4.3 \times 10^{11} \text{ m}^3 \text{ s}^{-1}$ ,  $Q_h = 4.35 \times 10^{11} \text{ m}^3 \text{ s}^{-1}$ ,  $Q_t = 4.37\text{--}4.97 \times 10^{11} \text{ m}^3 \text{ s}^{-1}$ , and  $Q_{2/3} = 3.95 \times 10^{11} \text{ m}^3 \text{ s}^{-1}$ , assuming  $\lambda_{cs} = 0.2$  and  $N_f = 0.024 \text{ s}^{-1}$ . These suggest mass eruption rates of  $\sim 5 \times 10^9 \text{ kg s}^{-1}$  using theoretical formulations and constants from Suzuki and Koyaguchi [2009]; see their Equation 2 and Section 4.3d. The volumetric flux estimated here is in agreement with the estimates of Gupta et al. [2022] and Van Eaton et al. [2023]. Assuming that the vertical exit velocity of the gas and particles was  $\sim 200 \text{ m s}^{-1}$  the time to reach 22 km (an average cloud top height) is  $\sim 2$  minutes, which suggests that the main explosion occurred at 04:15 UTC in agreement with other reported results [Kulichkov et al. 2022; Matoza et al. 2022; Wright et al. 2022; Yuen et al. 2022; Horváth et al. 2024]. For the 1-minute data it was possible to determine the equivalent radii for the lower intrusion based on the 225 K isotherm. Supplementary Material 1 Figure S4 shows the radial spread as a function of time for the period 07:05 to 10:18 UTC together with (inset) the trajectory of the location of the centroid of the 225 K contour, after correction for parallax. The  $t^{2/3}$  and  $t$  (constant velocity) best fit lines are also shown. The volumetric flux is on the order of  $\sim 2 \times 10^{11} \text{ m}^3 \text{ s}^{-1}$ , as determined from both fits. The intrusion depth was assumed to be 15 km based on 3-D umbrella model simulations of very large eruptions [Suzuki and Koyaguchi 2009], however it should be noted that  $h_0$  is poorly constrained. The trajectory of the centroid

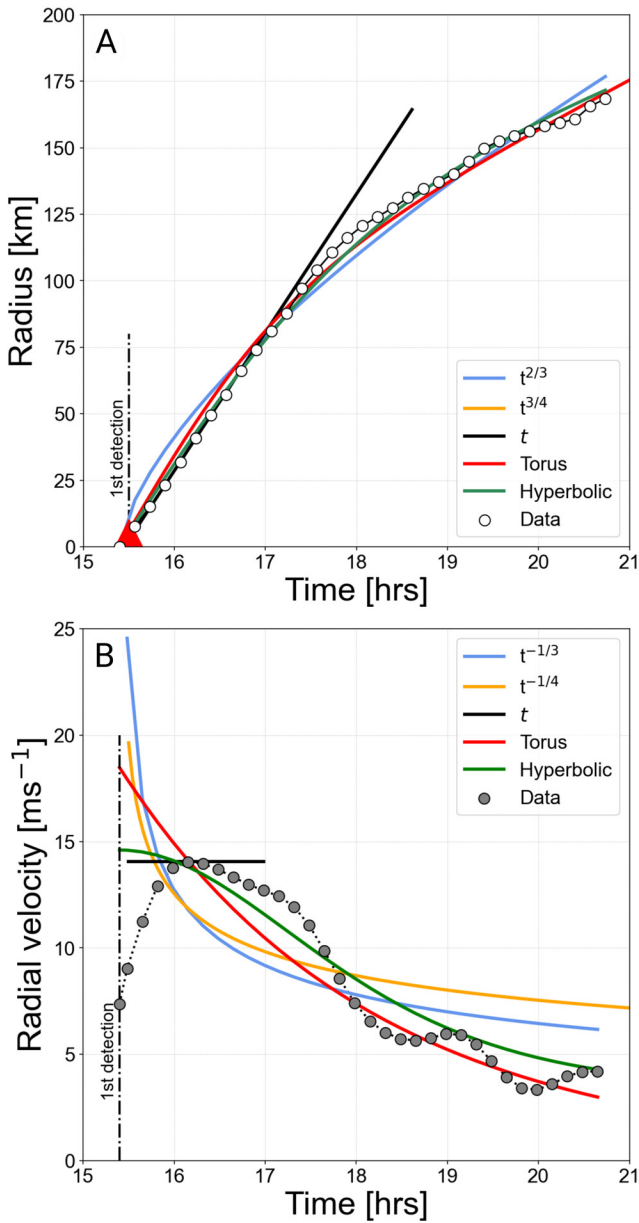


Figure 13: The Hunga eruption of 13 January 2022. [A] Radius as a function of time for the 13 January 2022 eruption of Hunga. Model fits for the constant velocity (black), hyperbolic (green) and torus (red) dependencies are shown (the torus model is very similar to the hyperbolic model in this case—see Figure 9T). Also shown are theoretical time dependencies based on the work of Pouget et al. [2016] for the initial gravity-driven regime  $t^{2/3}$  (blue) and  $t^{3/4}$  (orange). [B] Radial velocity,  $v_r$  as a function of time. The velocity dependences are shown with the same corresponding colours as the radius dependences (solid lines).

is almost due west and the umbrella intrusion radial velocity was determined to be  $\sim 31 \text{ m s}^{-1}$ .

#### 5.4 Spreading timescales

After a time-scale of  $\sim 3/N_f$  [Rooney and Devenish 2014], buoyancy-inertia forces take over and the radial spreading

continues, while the radial velocity decreases until finally the spreading dissipates. Three distinct flow regimes were modelled: a short period where the radial velocity is constant, a regime where the flow is buoyancy driven and  $r \sim t^{2/3}$  and a regime where the umbrella cloud is dissipating and  $r \sim t^{2/9}$ . To demonstrate the existence of the constant velocity regime, Figure 16 shows the temporal variation of the radial velocity of the mean of eight eruptions from Soufrière St Vincent on a logarithmic timescale to accentuate the initial time period. The  $t^{2/9}$  power law (not shown) tends to overestimate the spreading at the start of the eruption and is not a significant improvement in the dissipating stage and is not considered further. The torus model provides a better fit, generally, than the constant or  $t^{2/3}$  models and the hyperbolic model also gives a good fit for the entire timeline of the flow regimes. These data are at 1-minute time sampling and so can reliably capture the flow at sufficient time resolution to identify flow in the first few minutes after the eruptions. Note that these eruptions were all very similar in their propagation character. The grey-shaded region shows  $\pm 1\sigma$  around the mean line. The hyperbolic model predicts the constant velocity regime duration, whereas the power law ( $t^{2/3}$ ) fails to capture this flow regime. In their modelling, Ichihara et al. [2023] find a flow regime with  $r \propto t$  at the start of the Hunga 15 January 2022 eruption and  $r \propto t^{0.7}$  later. Suzuki and Koyaguchi [2009] used a 3D numerical model and also found a constant velocity flow at the start of their simulations (see their Figure 9a, and 9b) lasting  $\sim 500\text{--}800 \text{ s}$ . To examine the behaviour of the 15 January 2022 Hunga umbrella cloud radial velocity at later times, the 1-minute ABI data are plotted together with the AHI 10-minute observations for a period of  $\sim 3$  hours from 07:00 UTC (Figure 17). There is good correspondence between the AHI and ABI observations for this period, although the 1-minute data exhibits much greater variability. As discussed earlier the velocity variation can be simulated well using the hyperbolic model with an assumed eruption beginning at  $04:47 \pm 3$  minutes (UTC) (green-coloured line in Figure 17). The small amplitude oscillations in the ABI velocities have a frequency of  $\sim 1 \text{ mHz}$  and may be associated with the turbulent eddy turnover timescale of  $3 \text{ mHz}$  noted by Ichihara et al. [2023].

#### 5.5 Volumetric fluxes

The expression derived by Rooney and Devenish [2014] (their Equation 17a), can be used to estimate the volumetric flux at the start of the eruption (the constant velocity regime),

$$r(t) \approx \frac{Q_c}{2\pi r_0 h_0} t \sim O(N_f^{-1} t), \quad (22)$$

where  $Q_c$  is the volume flux ( $\text{m}^3 \text{ s}^{-1}$ ) and  $r_0, h_0$  are the initial umbrella radius and intrusion depth, respectively. Values of  $Q_c$  determined from Equation 10 and the values used for the  $r$  versus  $t$  relation are provided in Table 2 assuming an intrusion depth, that differs between eruptions. These estimates do not rely on any assumed parameters, e.g. entrainment and scaling coefficients or a value of  $N_f$  [Webster et al. 2020], other than the depth of the intrusion. Since  $Q_c$  scales with  $h_0$ , and  $h(t)$  decreases with time, a maximum volume flux can be determined by assuming an initial intrusion depth. This linear

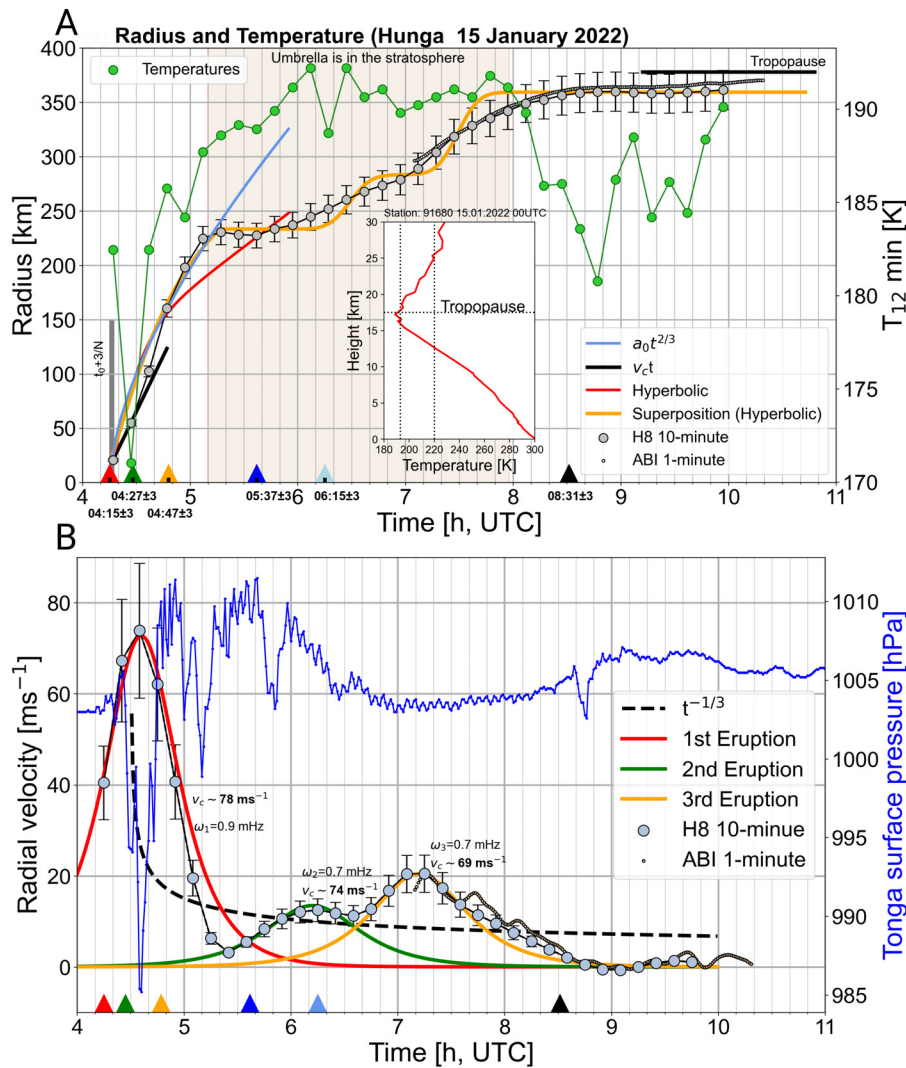


Figure 14: [A] Radius as a function of time for the 15 January 2022 eruption of Hunga determined from 10-minute AHI data. The coloured triangles along the abscissa indicate the times of eruptions deduced from the data. Fits based on  $t^{2/3}$ , hyperbolic and  $t$  (constant velocity) are shown to indicate that none of the models can properly fit the complete time history of the radial spread, assuming a single explosive event. [B] Radial velocity,  $v_r$  and surface pressure as a function of time. The surface pressure measurements [Wright et al. 2022] at Tonga,  $\sim 70$  km to the south, are shown (right-hand ordinate) to indicate the timings of the passage of the pressure drops associated with volcanic explosions. Individual fits using the hyperbolic model are shown for three assumed eruptions, colour coded according to the event. The orange-coloured line in [A] shows a superposition of these three hyperbolic model fits to the radial spread based on parameters that fit the  $v_r$  variation.

time-dependent regime appears to last much longer than expected from theory. Comparisons between the constant velocity flux ( $Q_c$ ) and  $Q_{2/3}$  from the  $t^{2/3}$  relation show reasonable agreement (Table 2); certainly well within the errors associated with calculating either value. The advantage of using the constant velocity estimate is significant, as only two data points are required and these necessarily need to be within a few minutes of the start of the eruption. However, it should be emphasised that the intrusion depth is an assumed parameter and its precise value controls these estimates of the volumetric flux. Aubry et al. [2019] simulated plumes for a large variety of conditions with a 3D plume model (ASHEE), and found that the vertical profile of horizontal mass flux into the umbrella cloud is well represented by a gaussian with width of 0.108 of

the plume height above vent level. This suggests an intrusion depth of  $0.22 (\pm 1\sigma)$  or  $0.43 (\pm 2\sigma)$  of the plume height [Aubry et al. 2019, see their Figure S2]. While certain physical constraints on its value can be made, observations, for example from a space based lidar [Winker et al. 2009], would be highly beneficial at the leading edges of the intrusion where the cloud is not optically thick.

Based on the models, a quantitative comparison between the volume flux estimates is shown in Figure 18. There is good correlation between the estimates over three orders of magnitude, and it appears that all of the models provide similar estimates, within the errors (shown as rectangular shaded regions surrounding the values). The one exception is the case of continuous emissions from Krakatau, where the  $t^{2/3}$

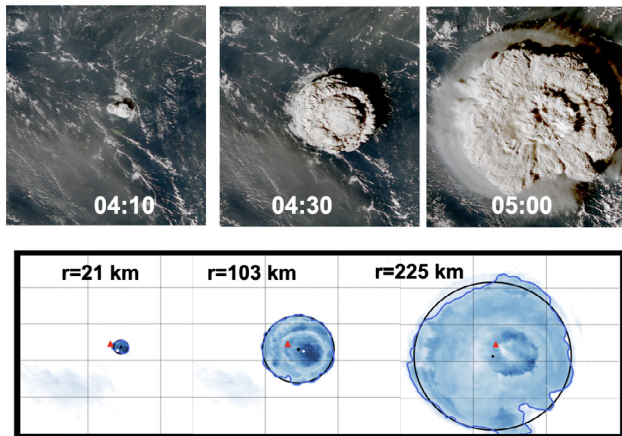


Figure 15: AHI images (true-colour) for the first ~1 hour following the first paroxysmal eruption of Hunga on 15 January 2022. The AHI sensor detected the eruption at 04:17 UT, ~2 minutes after the initial eruption. The lower panels show the CAER analyses at three different times with estimated radii illustrating the near-circularity of the initial (lower) umbrella cloud. The true-colour AHI images clearly show a second, lower altitude intrusion beginning to spread radially (04:50–05:00 UT).

model significantly underestimates the flux compared to the other models. The reason for this is that the radial spreading rate is more or less constant ( $\propto t$ ) as may be seen from the  $v_r$  plot (Figure 9); the new hyperbolic parametrisation is better able to model this type of emission. The correlation between volume flux and height is poor; suggesting that using height to estimate flux is unreliable (Figure 19). Likewise, correlations between flux, maximum radial velocity and maximum radius reached are also poor. The poor correlation between  $Q$  and maximum radius reached may be explained by noting that umbrella expansion at later times is also controlled by the background wind strength relative to the umbrella radial velocity and the effect of mixing, which reduces the brightness temperature contrast between the umbrella's leading edge and the background atmosphere.

The torus model parametrisation can be used to estimate the rate of decay of the flux with time. Although the form of the time dependence is prescribed, the rate of change is determined from the parameter  $\alpha$ , which was determined from the data fits. The decay rate is shown in Figure 20 for five different eruptions, from the longest lived (~12 hours for Pinatubo) to the short-lived (~1 hour) eruptions of Soufrière St Vincent and the Grenadines (SVG).

## 6 DISCUSSION AND CONCLUSIONS

It may be possible to reliably estimate the volumetric flux rapidly or within ~10–20 minutes after the initial eruption. The idea of using just the first few measurements to obtain an estimate of  $Q$  requires high time resolution data; at least 10 minute intervals, but 1-minute or 5-minute data are preferable. Such data are now available from several geostationary satellites. To further emphasise this idea, 5-minute data from

the SEVIRI instrument were analysed for two small eruptions of Etna volcano on 21 May 2023. The results are shown in Figure 21 where only the fluxes from the  $t^{2/3}$  model and the constant velocity model were determined. The second eruption is inferred from the change in slope (increase) of the data at around 09:25 UTC and agrees with the volcanic tremor data reported by De Beni et al. [2024] that shows increases at ~07:00 UTC and 09:00–09:40 UTC. The fluxes determined for these two small eruptions are  $\sim 0.7\text{--}0.9 \times 10^8 \text{ m}^3\text{s}^{-1}$  for both the constant velocity and  $t^{2/3}$  models and in good agreement, well within the uncertainty of the prescribed parameters. However, the constant velocity estimate would be available ~5–10 minutes after the cloud reaches neutral buoyancy, whereas the  $t^{2/3}$  model would require a further ~30–60 minutes for a reliable estimate.

An objective method for identifying the radius of volcanic umbrella clouds in light winds using infrared satellite-derived brightness temperature measurements is presented. The methodology is used to determine volcanic umbrella cloud structure, utilising well-established digital image processing techniques. A recipe for identifying umbrella clouds in thermal infrared satellite data was also proposed. It is not suggested that this is the only way of analysing the data nor is it suggested that the methods are optimised; the main purpose is to provide an objective and standardised means for describing volcanic umbrella clouds. A secondary purpose is to stimulate more work in this area and find improved objective ways to use the copious amounts of open-access satellite data now available.

By examining these data for the radial spreading of 13 volcanoes with large eruptions that produced near-circular umbrella clouds it was found that at the onset of the spreading, the radial velocity is almost constant and then decreases more slowly than expected from asymptotic power laws ( $\sim t^f$ ,  $f < 1$ ) deduced from gravity current theory. A new parametrisation involving the hyperbolic tangent function is proposed that captures the time history of radial spreading with a single parametrisation. However, it is not obvious how to estimate a volume flux from this relation. A theoretically justified model, based on a torus-shaped intrusion is proposed that provides good fits to the radial spreading and also improves the form of the radial velocity change with time and distance. This model is used to estimate the volume flux by determining its coefficients by fitting with measurements.

The two new models proposed are not necessarily specific to volcanic umbrella clouds: any atmospheric impulse that generates a large and vertically extended cloud should cause radial spreading according to the theory outlined here. An analysis of many large convective storms has been conducted to confirm this speculation and Figure 22 shows one example from data for a storm nicknamed 'Hector' (on the Tiwi islands, Northern Australia). Note that as in the case for the continuous phase of the 2018–2019 Krakatau activity, the radial spreading increases and the radial expansion velocity slowly decreases. This feature distinguishes short duration explosive events from more continuous convective cloud generation. The assumption that  $Q$  decays exponentially with time could be changed to a linear decay or some other form.

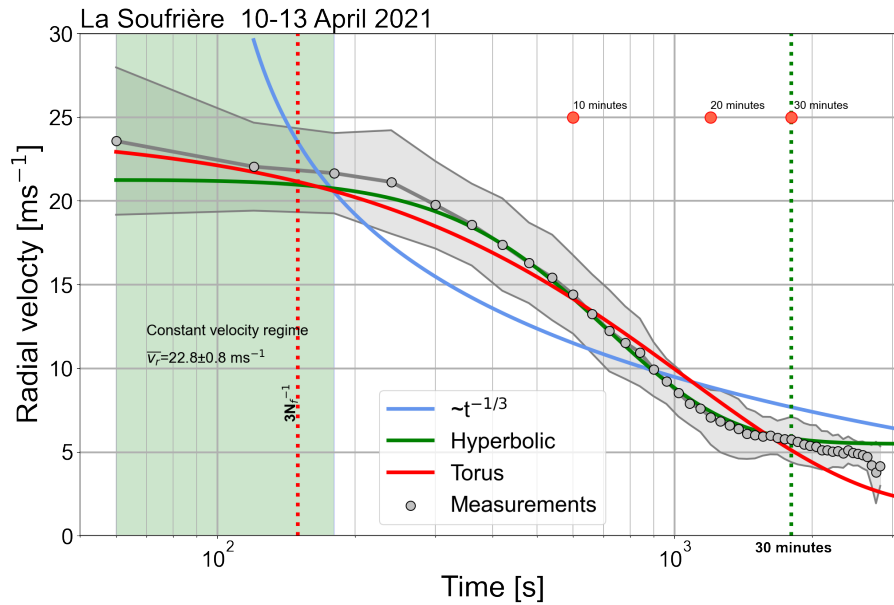


Figure 16: Mean radial velocity as a function of time for 1-minute data for eight separate eruptions of Soufrière St Vincent (La Soufrière). The vertical red dashed line shows the theoretically expected timescale for the constant velocity regime, in this case  $\sim 150$  s. Also shown are fits for the  $t^{2/3}$  (blue), hyperbolic (green) and torus (red) models. The grey-shaded region shows  $\pm 1\sigma$  around the mean line.

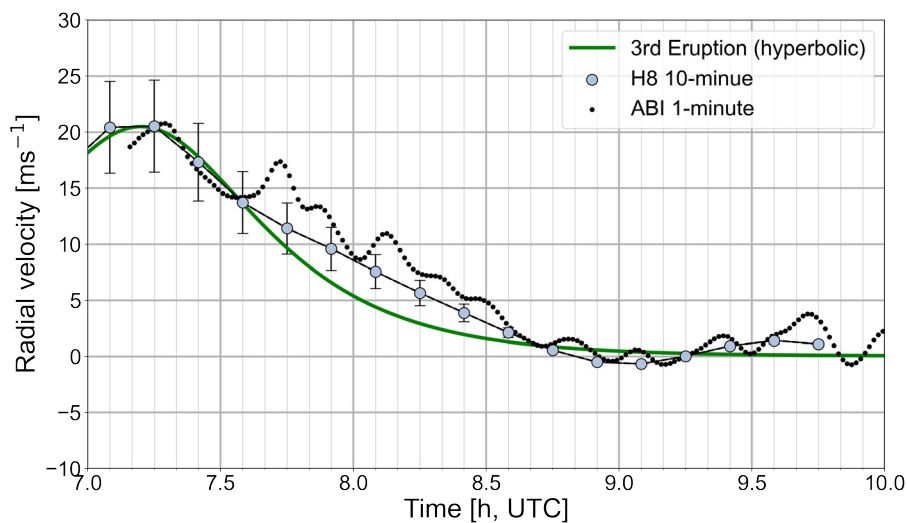


Figure 17: Velocity variation of the 15 January 2022 Hunga eruption from 07:00–10:00 UTC. The small blue-coloured dots are ABI 1-minute observations and the larger light-blue-coloured dots are 10-minute AH1 observations. The fit using the hyperbolic model using an eruption time of 04:47 UTC is shown as an orange line.

In the case of a continuous source some other dissipative process must operate on longer time scales. Previous work [e.g. Rooney and Devenish 2014] has assumed that  $h \sim \exp(-\beta t)$ , where  $\beta$  is related to  $N_f$ . The fits shown in Figure A5 suggest that the intrusion thins as  $\sim \text{sech}(\omega t)$ . It is entirely possible that the radial spread is very sensitive to the exact shape of the leading edge of the intrusion, in the case of volcanic intrusions, and better measurement data (3D) might reveal what the leading edge looks like.

A constant velocity regime has been found which does not last long, perhaps a few minutes and no more than a few tens

of minutes, that would be difficult to detect in hourly sampled satellite imagery and hence not previously reported. The existence of this regime has been theoretically predicted and observed in laboratory data [Kotsovinos 2000], but as far as we know this is the first time it has been studied for volcanic intrusions using satellite data. This has been made possible by the use of 1–10 minute sampled satellite-derived brightness temperatures. By examining the temporal evolution of the radial velocity, the presence of other eruptive events can be easily discerned. The constant velocity regime can be used to derive the volumetric flux ( $Q_c$ ) at the start of the eruption and

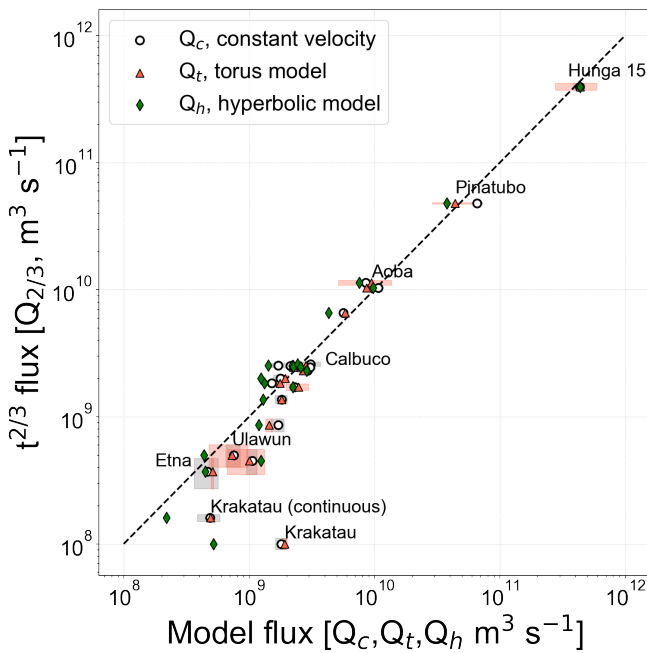


Figure 18: Comparison between volume flux estimates by different methods. The ordinate shows the flux estimates using the  $t^{2/3}$  variation ( $Q$ ; the abscissa shows the torus model ( $Q_t$ , blue circles) and the constant velocity model ( $Q_c$ , red circles). The shaded rectangular region surrounding each point is the estimated error.

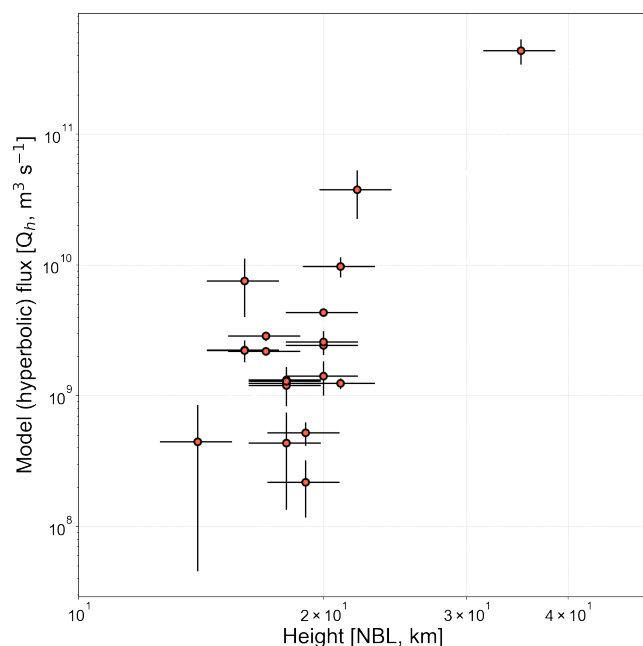


Figure 19: Height versus volumetric flux (hyperbolic model) for the explosive eruptions considered in this study. The best fits (not shown) suggests the correlations, with and without the Hunga 15 January 2022 eruption are poor ( $r^2 \leq 0.5$ ). Very similar low correlations are found for  $Q_{2/3}$  and  $Q_t$ .

is constrained by just one unknown: the intrusion depth. This may be a very useful result for modellers as generally  $Q$  (or

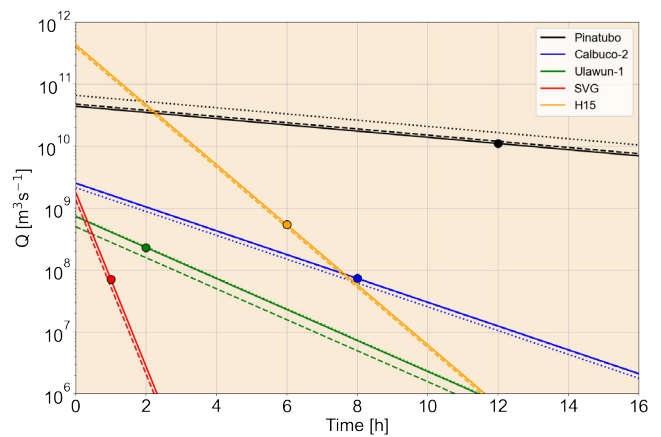


Figure 20: Rate of decay of the volumetric flux ( $Q$ ) as a function of time for five different eruptions. The solid line shows  $Q_t$ , the dashed-line shows  $Q$  and the dotted line shows  $Q_c$ .

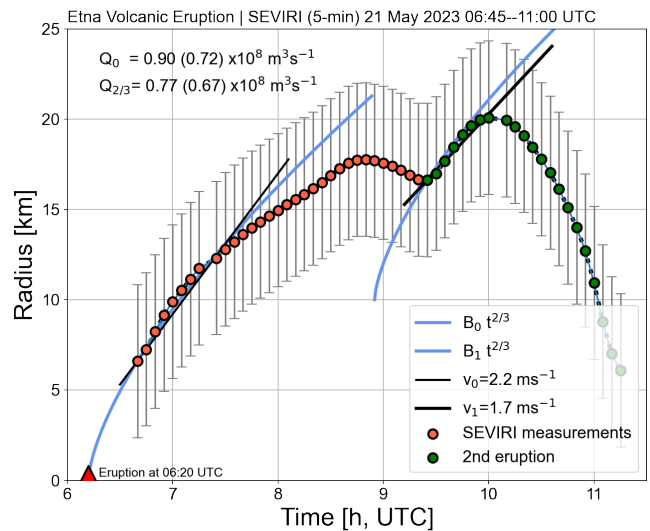


Figure 21: Estimating fluxes using the constant velocity assumption for two small eruptions of Etna on 21 May 2023. The constant velocity fluxes are estimated from the rate of change of the first 2 or 3 measurements of the radius (the slope or initial radial velocity), an assumed intrusion depth ( $h_0 = 1$  km, here) and the radius of the initial umbrella cloud,  $r_0$  (6.6 km, here). The  $t^{2/3}$  flux assumes  $\lambda_{CS} = 0.2$  and  $\bar{N} = 0.014$  (8–11 km) calculated from a radiosonde at Trapani (Station id: 16429, ~300 km due west of Etna).

the MER) is not known but is needed to provide accurate dispersion forecasts. Estimating  $Q$  from a power law model (e.g.  $t^{2/3}$ ) requires a much longer series of data points and hence a longer time to provide the estimate. The determination of  $Q$  this way still requires a value for an assumed parameter  $\lambda_{CS}$  (a cloud shape factor) that is poorly constrained and is variously assumed to have a value between 0.1–0.2 ( $\lambda_{CS} = 0.2$  has been assumed here). MER is then calculated from  $Q$  using, for example, the method in Van Eaton et al. [2016] (their Equation 1 and 2), which requires two more assumed parameters, an entrainment value and an empirical constant.

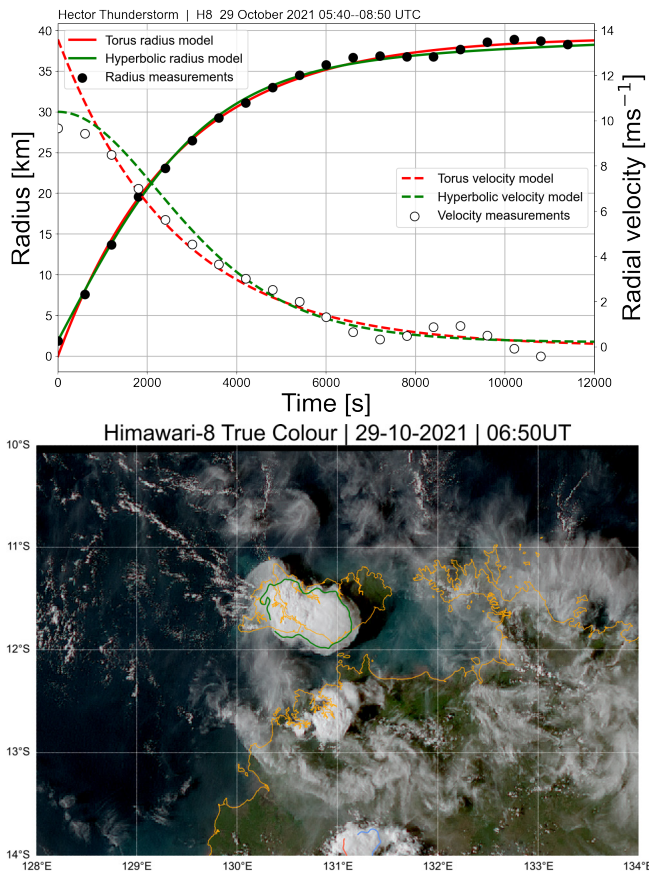


Figure 22: ‘Hector the Convectur’ storm analysis on 29 October 2021. Top: Radius and velocity (radial) versus time with the torus (red) and hyperbolic (green) model fits. The time axis has been changed to logarithmic to accentuate the difference in behaviour at the start of the spreading. Bottom: True colour Himawari-8 image of Hector at 06:50 UT (29/10/2021). The green-coloured contour is the 220 K isotherm based on 12  $\mu\text{m}$  brightness temperatures. The equivalent radius data were derived using the 220 K contour on consecutive 10 minute interval images.

The MER is sometimes calculated from a relation involving the plume-top neutral buoyancy height which has a power-law relationship for very large eruptions [Mastin et al. 2009]. This relation appears to be a consequence of the eruption process rather than fundamental to it, and was found to be poor ( $r^2 = 0.1\text{--}0.5$ ) for the cases studied here. Measurements of a spreading umbrella cloud and the rate at which it spreads, encapsulates, in a realistic way, the causal relation between the vertical momentum that creates the intrusion and its subsequent horizontal spreading. This seems to be a more robust way to estimate volume fluxes.

An interesting result of our analyses is the reasonable fits (radius versus time) obtained for the complete time-cycle of the intrusion based on the hyperbolic tangent function. The velocity versus time fits are found to be good when using the derivative of the hyperbolic tangent function. While no significant meaning has been placed on this result there remains the possibility that the intrusion behaves like a propagating

torus-shaped wavefront. The vertical momentum of the column and subsequent sloughing back into the troposphere generates wave motions that affect the radial spread. In a numerical model of umbrella cloud spreading, Suzuki and Koyaguchi [2009] found large amplitude wave structures in density, temperature and pressure at the top of the intrusion. They suggest that these wave-like perturbations occur around the neutral buoyancy level and that their characteristic frequency ( $\sim 3.1$  mHz) is related to the Brunt-Väisälä frequency in the stratified environment. The estimated frequencies found for the hyperbolic tangent fits are on the order of 0.1–0.9 mHz. Ichihara et al. [2023] propose that turbulent inertial particle clustering is responsible for the generation and spatial structure of the lightning rings [Van Eaton et al. 2023; Jarvis et al. 2024] observed during the 15 January 2022 Hunga eruption. The timescale of these turbulent eddies is 3 mHz.

The functional fits to  $v_r$  presented here follow closely the form  $\text{sech}^2(\omega t)$ . The maximum radial speeds found for the umbrella clouds range from 10–79  $\text{ms}^{-1}$ , which implies a large range of intrusion depths  $h$  of  $\sim 1$  to 15 km. The very high  $v_r$  of the Hunga eruption, corresponds to a large volumetric flow rate and deep intrusion which are consistent with this eruption being thermally energetic [Wright et al. 2022]. Finally, this work suggests that high cadence satellite measurements of powerful eruptions and also of large convective storm systems are useful for determining volumetric flow rates directly and, in the case of eruptions, by assuming a constant velocity phase at the start of the eruption, a rapid estimate of  $Q$  is possible. This information will be useful for initiating models that forecast the dispersion of volcanic material in the atmosphere.

## AUTHOR CONTRIBUTIONS

FP conceived the study, analysed the data and wrote most of the paper. AP analysed data, provided code, checked the analysis and contributed to writing the paper. MB and FP devised the model and contributed to writing the paper. RG and TA checked the analysis, contributed to conceptualisation and helped write the paper. RT provided the statistical analyses, organised the Excel data and contributed to writing the paper.

## ACKNOWLEDGEMENTS

R. Tanner is supported by a DTP studentship from the UK Engineering and Physical Sciences Research Council. The authors are grateful to the satellite data providers (NASA/Eumetsat/ESA/JMA/JAXA), and especially JMA/JAXA for access to the Himawari AHI data used extensively in this study. Two anonymous reviewers provided very helpful and constructive comments for which we are most grateful. In particular one reviewer is thanked for a comprehensive analysis of our paper and for directing us to several important papers which we had overlooked.

## DATA AVAILABILITY

The 10- and 1-minute satellite data used in this study are available freely from amazon web services. Himawari: <https://registry.opendata.aws/noaa-himawari/>.

ABI: <https://registry.opendata.aws/collab/noaa/>. MODIS Level 1: <https://ladsweb.modaps.eosdis.nasa.gov/missions-and-measurements/science-domain/modis-L0L1/>. Level 1.5 MSG/SEVIRI data can be obtained from <https://data.eumetsat.int/data/>. Radiosonde data (used to calculate  $N_f$ ) are available from <https://weather.uwyo.edu/upperair/sounding.html>. The analysed umbrella cloud brightness temperature radius and velocities are provided in an Excel file as well as all of the model fits and derived parameters.

## COPYRIGHT NOTICE

© The Author(s) 2025. This article is distributed under the terms of the [Creative Commons Attribution 4.0 International License](https://creativecommons.org/licenses/by/4.0/), which permits unrestricted use, distribution, and reproduction in any medium, provided you give appropriate credit to the original author(s) and the source, provide a link to the Creative Commons license, and indicate if changes were made.

## REFERENCES

- Allen, T. (2013). *Particle size measurement*. Springer Dordrecht. 806 pages. DOI: [10.1007/978-94-009-0417-0](https://doi.org/10.1007/978-94-009-0417-0).
- Aubry, T. J., M. Cerminara, and A. M. Jellinek (2019). “Impacts of climate change on volcanic stratospheric injections: comparison of 1-D and 3-D plume model projections”. *Geophysical Research Letters* 46(17-18), pages 10609–10618. DOI: [10.1029/2019GL083975](https://doi.org/10.1029/2019GL083975).
- Aubry, T. J., S. L. Engwell, C. Bonadonna, L. G. Mastin, G. Carazzo, A. R. Van Eaton, D. E. Jessop, R. G. Grainger, S. Scollo, I. A. Taylor, et al. (2023). “New insights into the relationship between mass eruption rate and volcanic column height based on the IVESPA data set”. *Geophysical Research Letters* 50(14), e2022GL102633. DOI: [10.1029/2022GL102633](https://doi.org/10.1029/2022GL102633).
- Baines, P. and R. Sparks (2005). “Dynamics of giant volcanic ash clouds from supervolcanic eruptions”. *Geophysical Research Letters* 32(24). DOI: [10.1029/2005GL024597](https://doi.org/10.1029/2005GL024597).
- Basilio Hazas, M., F. Ziliotto, J. Lee, M. Rolle, and G. Chiogna (2023). “Evolution of plume geometry, dilution and reactive mixing in porous media under highly transient flow fields at the surface water-groundwater interface”. *Journal of Contaminant Hydrology* 258, page 104243. DOI: [10.1016/j.jconhyd.2023.104243](https://doi.org/10.1016/j.jconhyd.2023.104243).
- Bear-Crozier, A., S. Pouget, M. Bursik, E. Jansons, J. Denman, A. Tupper, and R. Rustowicz (2020). “Automated detection and measurement of volcanic cloud growth: towards a robust estimate of mass flux, mass loading and eruption duration”. *Natural Hazards* 101(1), pages 1–38. DOI: [10.1007/s11069-019-03847-2](https://doi.org/10.1007/s11069-019-03847-2).
- Benjamin, T. B. (1968). “Gravity currents and related phenomena”. *Journal of Fluid Mechanics* 31(2), pages 209–248. DOI: [10.1017/s0022112068000133](https://doi.org/10.1017/s0022112068000133).
- Bursik, M. I., S. N. Carey, and R. S. J. Sparks (1992). “A gravity current model for the May 18, 1980 Mount St. Helens plume”. *Geophysical Research Letters* 19(16), pages 1663–1666. DOI: [10.1029/92gl01639](https://doi.org/10.1029/92gl01639).
- Canny, J. (1986). “A computational approach to edge detection”. *IEEE Transactions on pattern analysis and machine intelligence* PAMI-8(6), pages 679–698. DOI: [10.1109/TPAMI.1986.4767851](https://doi.org/10.1109/TPAMI.1986.4767851).
- Carey, S. and M. Bursik (2015). “Volcanic Plumes”. *The Encyclopedia of Volcanoes*. Edited by H. Sigurdsson. 2nd edition. Elsevier, pages 571–585. ISBN: 9780123859389. DOI: [10.1016/b978-0-12-385938-9.00032-8](https://doi.org/10.1016/b978-0-12-385938-9.00032-8).
- Carn, S. A., N. A. Krotkov, B. L. Fisher, and C. Li (2022). “Out of the blue: Volcanic SO<sub>2</sub> emissions during the 2021–2022 eruptions of Hunga Tonga—Hunga Ha’apai (Tonga)”. *Frontiers in Earth Science* 10. DOI: [10.3389/feart.2022.976962](https://doi.org/10.3389/feart.2022.976962).
- Carr, J. L., Á. Horváth, D. L. Wu, and M. D. Friberg (2022). “Stereo Plume Height and Motion Retrievals for the Record-Setting Hunga Tonga-Hunga Ha’apai Eruption of 15 January 2022”. *Geophysical Research Letters* 49(9), e2022GL098131. DOI: [10.1029/2022GL098131](https://doi.org/10.1029/2022GL098131).
- Chassignet, E. P., C. Cenedese, and J. Verron (2012). *Buoyancy-driven flows*. Cambridge: Cambridge University Press. 444 pages. ISBN: 978-1-107-00887-8. DOI: [10.1017/CB09780511920196](https://doi.org/10.1017/CB09780511920196).
- Constantinescu, R., A. Hopulele-Gligor, C. B. Connor, C. Bonadonna, L. J. Connor, J. M. Lindsay, S. Charbonnier, and A. Volentik (2021). “The radius of the umbrella cloud helps characterize large explosive volcanic eruptions”. *Communications Earth & Environment* 2(1), pages 1–8. DOI: [10.1038/s43247-020-00078-3](https://doi.org/10.1038/s43247-020-00078-3).
- Costa, A., A. Folch, G. Macedonio, B. Giaccio, R. Isaia, and V. C. Smith (2012). “Quantifying volcanic ash dispersal and impact of the Campanian Ignimbrite super-eruption”. *Geophysical Research Letters* 39(10). DOI: [10.1029/2012GL051605](https://doi.org/10.1029/2012GL051605).
- Costa, A., A. Folch, and G. Macedonio (2013). “Density-driven transport in the umbrella region of volcanic clouds: Implications for tephra dispersion models”. *Geophysical Research Letters* 40(18), pages 4823–4827. DOI: [10.1002/grl.50942](https://doi.org/10.1002/grl.50942).
- De Beni, E., C. Proietti, S. Scollo, M. Cantarero, L. Mereu, F. Romeo, L. Pioli, M. Sciotto, and S. Alparone (2024). “A Hidden Eruption: The 21 May 2023 Paroxysm of the Etna Volcano (Italy)”. *Remote Sensing* 16(9), page 1555. DOI: [10.3390/rs16091555](https://doi.org/10.3390/rs16091555).
- Didden, N. and T. Maxworthy (1982). “The viscous spreading of plane and axisymmetric gravity currents”. *Journal of Fluid Mechanics* 121(1), page 27. DOI: [10.1017/s0022112082001785](https://doi.org/10.1017/s0022112082001785).
- Ernst, G. G. J., R. S. J. Sparks, S. N. Carey, and M. I. Bursik (1996). “Sedimentation from turbulent jets and plumes”. *Journal of Geophysical Research: Solid Earth* 101(B3), pages 5575–5589. DOI: [10.1029/95jb01900](https://doi.org/10.1029/95jb01900).
- Feret, L. R. (1930). “La grosseur des grains des matières pulvérulentes”. *Premières Communications de la Nouvelle Association Internationale pour l’Essai des Matériaux* 2(Group D), pages 428–436.
- Fischer, H. B., E. J. List, R. C. Y. Koh, J. Imberger, and N. H. Brooks (1979). “Mixing in rivers”. *Mixing in inland and coastal waters*. Elsevier. Chapter 5, pages 104–147. ISBN: 9780080511771. DOI: [10.1016/c2009-0-22051-4](https://doi.org/10.1016/c2009-0-22051-4).

- Flynn, M. R. and B. R. Sutherland (2004). “Intrusive gravity currents and internal gravity wave generation in stratified fluid”. *Journal of Fluid Mechanics* 514, pages 355–383. DOI: [10.1017/s0022112004000400](https://doi.org/10.1017/s0022112004000400).
- George, W. K. (1989). “The self-preservation of turbulent flows and its relation to initial conditions and coherent structures”. *Advances in turbulence* 3973, pages 39–73.
- Gill, A. E. (1981). “Homogeneous intrusions in a rotating stratified fluid”. *Journal of Fluid Mechanics* 103(1), page 275. DOI: [10.1017/s0022112081001341](https://doi.org/10.1017/s0022112081001341).
- Gonzalez, R. and R. Woods (2017). *Digital Image Processing*. 4th edition. Pearson Education Limited. 1024 pages. ISBN: 9781292223049.
- Gupta, A. K., R. Bennartz, K. E. Fauria, and T. Mittal (2022). “Eruption chronology of the December 2021 to January 2022 Hunga Tonga-Hunga Ha’apai eruption sequence”. *Communications Earth & Environment* 3(1). DOI: [10.1038/s43247-022-00606-3](https://doi.org/10.1038/s43247-022-00606-3).
- Hargie, K. A., A. R. Van Eaton, L. G. Mastin, R. H. Holzworth, J. W. Ewert, and M. Pavolonis (2019). “Globally detected volcanic lightning and umbrella dynamics during the 2014 eruption of Kelud, Indonesia”. *Journal of Volcanology and Geothermal Research* 382, pages 81–91. DOI: [10.1016/j.jvolgeores.2018.10.016](https://doi.org/10.1016/j.jvolgeores.2018.10.016).
- Heywood, H. (1933). “Calculation of the specific surface of a powder”. *Proceedings of the Institution of Mechanical Engineers* 125(1), pages 383–459. DOI: [10.1243/PIME\\_PROC\\_1933\\_125\\_021\\_02](https://doi.org/10.1243/PIME_PROC_1933_125_021_02).
- Hofer, L. R., M. Krstajić, and R. P. Smith (2022). “JAXFit: Trust Region Method for Nonlinear Least-Squares Curve Fitting on the GPU”. *arXiv* 2208.12187. DOI: [10.48550/arXiv.2208.12187](https://doi.org/10.48550/arXiv.2208.12187). [preprint].
- Holasek, R. E., S. Self, and A. W. Woods (1996). “Satellite observations and interpretation of the 1991 Mount Pinatubo eruption plumes”. *Journal of Geophysical Research: Solid Earth* 101(B12), pages 27635–27655. DOI: [10.1029/96jb01179](https://doi.org/10.1029/96jb01179).
- Horváth, Á., S. L. Vadas, C. C. Stephan, and S. A. Buehler (2024). “One-Minute Resolution GOES-R Observations of Lamb and Gravity Waves Triggered by the Hunga Tonga-Hunga Ha’apai Eruptions on 15 January 2022”. *Journal of Geophysical Research: Atmospheres* 129(3). DOI: [10.1029/2023jd039329](https://doi.org/10.1029/2023jd039329).
- Huppert, H. E. (2006). “Gravity currents: a personal perspective”. *Journal of Fluid Mechanics* 554(1), page 299. DOI: [10.1017/s002211200600930x](https://doi.org/10.1017/s002211200600930x).
- Ichihara, M., P. D. Mininni, S. Ravichandran, C. Cimarelli, and C. Vagasky (2023). “Multiphase turbulent flow explains lightning rings in volcanic plumes”. *Communications Earth & Environment* 4(1). DOI: [10.1038/s43247-023-01074-z](https://doi.org/10.1038/s43247-023-01074-z).
- Jarvis, P. A., T. G. Caldwell, C. Noble, Y. Ogawa, and C. Vagasky (2024). “Volcanic lightning reveals umbrella cloud dynamics of the 15 January 2022 Hunga volcano eruption, Tonga”. *Bulletin of Volcanology* 86(6). DOI: [10.1007/s00445-024-01739-3](https://doi.org/10.1007/s00445-024-01739-3).
- Johnson, C. G., A. J. Hogg, H. E. Huppert, R. S. J. Sparks, J. C. Phillips, A. C. Slim, and M. J. Woodhouse (2015). “Modelling intrusions through quiescent and moving ambients”. *Journal of Fluid Mechanics* 771, pages 370–406. DOI: [10.1017/jfm.2015.180](https://doi.org/10.1017/jfm.2015.180).
- Kotsovinos, N. E. (2000). “Axisymmetric submerged intrusion in stratified fluid”. *Journal of Hydraulic Engineering* 126(6), pages 446–456. DOI: [10.1061/\(ASCE\)0733-9429\(2000\)126:6\(446\)](https://doi.org/10.1061/(ASCE)0733-9429(2000)126:6(446)).
- Kroell, N. (2021). “imea: A Python package for extracting 2D and 3D shape measurements from images”. *Journal of Open Source Software* 6(60), page 3091. DOI: [10.21105/joss.03091](https://doi.org/10.21105/joss.03091).
- Kulichkov, S., I. Chunchuzov, O. Popov, G. Gorchakov, A. Mishenin, V. Perepelkin, G. Bush, A. Skorokhod, Y. A. Vinogradov, E. Semutnikova, et al. (2022). “Acoustic-gravity Lamb waves from the eruption of the Hunga-Tonga-Hunga-Hapai Volcano, its energy release and impact on aerosol concentrations and tsunami”. *Pure and Applied Geophysics* 179(5), pages 1533–1548. DOI: [10.1007/s00024-022-03046-4](https://doi.org/10.1007/s00024-022-03046-4).
- Lombardi, V., C. Adduce, G. Sciortino, and M. La Rocca (2015). “Gravity currents flowing upslope: Laboratory experiments and shallow-water simulations”. *Physics of Fluids* 27(1). DOI: [10.1063/1.4905305](https://doi.org/10.1063/1.4905305).
- Martin, G., C. E. Blyth, and H. Tongue (1923). “Researches on the Theory of Fine Grinding. Part 1”. *Transactions of the British Ceramic Society* 23(2), pages 61–78.
- Mason, B. G., D. M. Pyle, and C. Oppenheimer (2004). “The size and frequency of the largest explosive eruptions on Earth”. *Bulletin of Volcanology* 66(8), pages 735–748. DOI: [10.1007/s00445-004-0355-9](https://doi.org/10.1007/s00445-004-0355-9).
- Mastin, L. G., M. Guffanti, R. Servranckx, P. Webley, S. Barsotti, K. Dean, A. Durant, J. W. Ewert, A. Neri, W. I. Rose, D. Schneider, L. Siebert, B. Stunder, G. Swanson, A. Tupper, A. Volentik, and C. F. Waythomas (2009). “A multidisciplinary effort to assign realistic source parameters to models of volcanic ash-cloud transport and dispersion during eruptions”. *Journal of Volcanology and Geothermal Research* 186(1-2), pages 10–21. DOI: [10.1016/j.jvolgeores.2009.01.008](https://doi.org/10.1016/j.jvolgeores.2009.01.008).
- Matoza, R. S., D. Fee, J. D. Assink, A. M. Iezzi, D. N. Green, K. Kim, L. Toney, T. Lecocq, S. Krishnamoorthy, J.-M. Lalande, et al. (2022). “Atmospheric waves and global seismoacoustic observations of the January 2022 Hunga eruption, Tonga”. *Science* 377(6601), pages 95–100. DOI: [10.1126/science.abo7063](https://doi.org/10.1126/science.abo7063).
- McKee, K., C. M. Smith, K. Reath, E. Snee, S. Maher, R. S. Matoza, S. Carn, D. C. Roman, L. Mastin, K. Anderson, D. Damby, I. Itikarai, K. Mulina, S. Saunders, J. D. Assink, R. de Negri Leiva, and A. Perttu (2021). “Evaluating the state-of-the-art in remote volcanic eruption characterization Part II: Ulawun volcano, Papua New Guinea”. *Journal of Volcanology and Geothermal Research* 420, page 107381. DOI: [10.1016/j.jvolgeores.2021.107381](https://doi.org/10.1016/j.jvolgeores.2021.107381).
- Newhall, C. G. and S. Self (1982). “The volcanic explosivity index (VEI) an estimate of explosive magnitude for historical volcanism”. *Journal of Geophysical Research: Oceans* 87(C2), pages 1231–1238. DOI: [10.1029/jc087ic02p01231](https://doi.org/10.1029/jc087ic02p01231).

- Pahl, M., G. Sschadel, and H. Rumpf (1973). “Zusammenstellung von Teilchenformbeschreibungsmethoden. I”. *Aufbereitungs-Technik* 2(5), pages 257–264.
- Pouget, S., M. Bursik, C. G. Johnson, A. J. Hogg, J. C. Phillips, and R. S. J. Sparks (2016). “Interpretation of umbrella cloud growth and morphology: implications for flow regimes of short-lived and long-lived eruptions”. *Bulletin of Volcanology* 78(1), pages 1–19. DOI: [10.1007/s00445-015-0993-0](https://doi.org/10.1007/s00445-015-0993-0).
- Pouget, S., M. Bursik, P. Webley, J. Dehn, and M. Pavolonis (2013). “Estimation of eruption source parameters from umbrella cloud or downwind plume growth rate”. *Journal of Volcanology and Geothermal Research* 258, pages 100–112. DOI: [10.1016/j.jvolgeores.2013.04.002](https://doi.org/10.1016/j.jvolgeores.2013.04.002).
- Prata, A. T., A. Folch, A. J. Prata, R. Biondi, H. Brenot, C. Cimarelli, S. Corradini, J. Lapierre, and A. Costa (2020). “Anak Krakatau triggers volcanic freezer in the upper troposphere”. *Scientific Reports* 10(1), pages 1–13. DOI: [10.1038/s41598-020-60465-w](https://doi.org/10.1038/s41598-020-60465-w).
- Prata, A. J. (1989). “Infrared radiative transfer calculations for volcanic ash clouds”. *Geophysical Research Letters* 16(11), pages 1293–1296. DOI: [10.1029/g1016i011p01293](https://doi.org/10.1029/g1016i011p01293).
- Proud, S. R., A. T. Prata, and S. Schmauß (2022). “The January 2022 eruption of Hunga Tonga-Hunga Ha’apai volcano reached the mesosphere”. *Science* 378(6619), pages 554–557. DOI: [DOI:10.1126/science.abo4076](https://doi.org/10.1126/science.abo4076).
- Rooney, G. and B. Devenish (2014). “Plume rise and spread in a linearly stratified environment”. *Geophysical & Astrophysical Fluid Dynamics* 108(2), pages 168–190. DOI: [10.1080/03091929.2013.849345](https://doi.org/10.1080/03091929.2013.849345).
- Szwarcz, H. and K. Shane (1969). “Measurement of particle shape by Fourier analysis”. *Sedimentology* 13(3–4), pages 213–231. DOI: [10.1111/j.1365-3091.1969.tb00170.x](https://doi.org/10.1111/j.1365-3091.1969.tb00170.x).
- Simpson, J. E. (1999). *Gravity currents: In the environment and the laboratory*. 2nd edition. Cambridge: Cambridge University Press. 244 pages. ISBN: 9780521561099.
- Sobel, I. and G. Feldman (1968). “A 3x3 Isotropic Gradient Operator for Image Processing”. DOI: [10.13140/RG.2.1.1912.4965](https://doi.org/10.13140/RG.2.1.1912.4965). Presented at the Stanford Artificial Intelligence Project (SAIL).
- Sparks, R. S. J., M. I. Bursik, S. N. Carey, J. Gilbert, L. Glaze, H. Sigurdsson, and A. Woods (1997). *Volcanic plumes*. John Wiley & Sons, Inc. ISBN: 0471939013.
- Sparks, R. S. J., S. N. Carey, and H. Sigurdsson (1991). “Sedimentation from gravity currents generated by turbulent plumes”. *Sedimentology* 38(5), pages 839–856. DOI: [10.1111/j.1365-3091.1991.tb01875.x](https://doi.org/10.1111/j.1365-3091.1991.tb01875.x).
- Sparks, R. S. J., J. G. Moore, and C. J. Rice (1986). “The initial giant umbrella cloud of the May 18th, 1980, explosive eruption of Mount St. Helens”. *Journal of Volcanology and Geothermal Research* 28(3–4), pages 257–274. DOI: [10.1016/0377-0273\(86\)90026-0](https://doi.org/10.1016/0377-0273(86)90026-0).
- Suzuki, Y. and T. Koyaguchi (2009). “A three-dimensional numerical simulation of spreading umbrella clouds”. *Journal of Geophysical Research: Solid Earth* 114(B03209). DOI: [10.1029/2007JB005369](https://doi.org/10.1029/2007JB005369).
- Tabata, T., V. O. John, R. A. Roebeling, T. Hewison, and J. Schulz (2019). “Recalibration of over 35 years of infrared and water vapor channel radiances of the JMA geostationary satellites”. *Remote Sensing* 11(10), page 1189. DOI: [10.3390/rs11101189](https://doi.org/10.3390/rs11101189).
- Thomas, H. E. and A. J. Prata (2018). “Computer vision for improved estimates of SO<sub>2</sub> emission rates and plume dynamics”. *International Journal of Remote Sensing* 39(5), pages 1285–1305. DOI: [10.1080/01431161.2017.1401250](https://doi.org/10.1080/01431161.2017.1401250).
- Ungarish, M. and T. Zemach (2007). “On axisymmetric intrusive gravity currents in a stratified ambient – shallow-water theory and numerical results”. *European Journal of Mechanics - B/Fluids* 26(2), pages 220–235. DOI: [10.1016/j.euromechflu.2006.06.003](https://doi.org/10.1016/j.euromechflu.2006.06.003).
- Van Eaton, A. R., Á. Amigo, D. Bertin, L. G. Mastin, R. E. Giacosa, J. González, O. Valderrama, K. Fontijn, and S. A. Behnke (2016). “Volcanic lightning and plume behavior reveal evolving hazards during the April 2015 eruption of Calbuco volcano, Chile”. *Geophysical Research Letters* 43(7), pages 3563–3571. DOI: [10.1002/2016gl068076](https://doi.org/10.1002/2016gl068076).
- Van Eaton, A. R., J. Lapierre, S. A. Behnke, C. Vagasky, C. J. Schultz, M. Pavolonis, K. Bedka, and K. Khlopenkov (2023). “Lightning rings and gravity waves: Insights into the giant eruption plume from Tonga’s Hunga Volcano on 15 January 2022”. *Geophysical Research Letters* 50(12), e2022GL102341. DOI: [10.1029/2022GL102341](https://doi.org/10.1029/2022GL102341).
- Webster, H. N., B. J. Devenish, L. G. Mastin, D. J. Thomson, and A. R. Van Eaton (2020). “Operational Modelling of Umbrella Cloud Growth in a Lagrangian Volcanic Ash Transport and Dispersion Model”. *Atmosphere* 11(2), page 200. DOI: [10.3390/atmos11020200](https://doi.org/10.3390/atmos11020200).
- Winker, D. M., M. A. Vaughan, A. Omar, Y. Hu, K. A. Powell, Z. Liu, W. H. Hunt, and S. A. Young (2009). “Overview of the CALIPSO Mission and CALIOP Data Processing Algorithms”. *Journal of Atmospheric and Oceanic Technology* 26(11), pages 2310–2323. DOI: [10.1175/2009jtecha1281.1](https://doi.org/10.1175/2009jtecha1281.1).
- Woods, A. (1988). “The fluid dynamics and thermodynamics of eruption columns”. *Bulletin of Volcanology* 50(3), pages 169–193. DOI: [10.1007/BF01079681](https://doi.org/10.1007/BF01079681).
- Woods, A. W. and J. Kienle (1994). “The dynamics and thermodynamics of volcanic clouds: theory and observations from the April 15 and April 21, 1990 eruptions of Redoubt Volcano, Alaska”. *Journal of Volcanology and Geothermal Research* 62(1–4), pages 273–299. DOI: [10.1016/0377-0273\(94\)90037-X](https://doi.org/10.1016/0377-0273(94)90037-X).
- Wright, C. J., N. P. Hindley, M. J. Alexander, M. Barlow, L. Hoffmann, C. N. Mitchell, F. Prata, M. Bouillon, J. Carstens, C. Clerboux, S. M. Osprey, N. Powell, C. E. Randall, and J. Yue (2022). “Surface-to-space atmospheric waves from Hunga Tonga–Hunga Ha’apai eruption”. *Nature* 609(7928), pages 741–746. DOI: [10.1038/s41586-022-05012-5](https://doi.org/10.1038/s41586-022-05012-5).
- Yuen, D. A., M. A. Scroggs, F. J. Spera, Y. Zheng, H. Hu, S. R. McNutt, G. Thompson, K. Mandli, B. R. Keller, S. S. Wei, Z. Peng, Z. Zhou, F. Mulargia, and Y. Tanioka (2022). “Under the surface: Pressure-induced planetary-scale waves, volcanic lightning, and gaseous clouds caused by the submarine eruption of Hunga Tonga-Hunga Ha’apai volcano”. *Earthquake Research Advances* 2(3), page 100134. DOI: [10.1016/j.eqrea.2022.100134](https://doi.org/10.1016/j.eqrea.2022.100134).

## APPENDIX A: IMAGE PROCESSING

A variety of tools were used to detect and define the size and shapes of umbrella clouds. The measures with examples are summarised here.

### A1 Edge detection

The Canny edge detector [Canny 1986] was used to determine the location of the edges of the selected brightness temperature isotherm. The method consists of multiple stages: noise reduction, filtering and gradient estimation using derivatives, checking for local maxima and thresholding. An example of the use of the algorithm is shown in Figure A1.

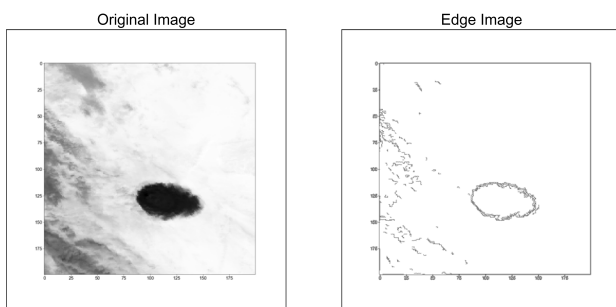


Figure A1: Canny edge detection applied to the Mt Etna MODIS 12  $\mu\text{m}$  brightness temperature image (see Figure 2).

### A2 Morphology

The morphological properties of cloud structures are analysed using a 2D shape extraction open source Python package (*imea*). A full description of over 50 different shape descriptors is provided by Kroell [2021]. For this work, the main interest is with the distortion of the cloud from a circular shape. The measures used are:

- The radius of the circle circumscribing the cloud shape
- The radius of the circle inscribing the cloud shape
- The Feret diameter [Feret 1930]. The greatest perpendicular distance (greatest Feret diameter–GFD) with parallel tangents touching opposite sides of the shape profile.
- The Horizontal Martin diameter [Martin et al. 1923]. A measure of the horizontal chord length that bisects the shape into two equal halves.
- The Nassenstein diameter [Pahl et al. 1973]. Corresponds to the length of a chord in the shape profile that is perpendicular to the tangent at the point of contact.
- The maximum chord length of the cloud shape.
- Heywood diameter [Heywood 1933]. This is the diameter of a circle that has the same area as the cloud shape.

An example of the morphological measures is shown in Figures A2 and A3. The statistical length is a measure of the chord length (or Feret, Martin, and Nassenstein diameters) as

a function of angle measured clockwise from the x-axis (horizontal). For example in Figure A2, the Feret diameter with angle = 0 degrees is 278 km. The diameter is measured as the orthogonal distance between the parallel lines (Figure A2, panels in second row). Rotating these lines through small steps in angle clockwise, and measuring the orthogonal distance gives a statistical length as a function of angle (Figure A2, panels in third row). The frequency distribution of statistical lengths is shown in Figure A2, fourth row.

This work utilised these measures in a subjective manner to assess the degree of distortion (from circular) of the umbrella clouds. In future work the shape distortion metrics will be used to objectively analyse the effects of winds, wind shear and horizontal mixing on propagating volcanic intrusions. The example for Taal (Figure A3) illustrates the shape metrics for a highly elongated plume-like cloud.

### A3 Shape factors

Shape factors are non-dimensional parameters, in this context, describing the shape of 2D cloud objects. The factors used are: *Circularity*  $C$  and the *Roundness*  $\mathcal{R}$ —see Equation 2 and Equation 3, respectively for the mathematical definitions. Both measures are intuitive and need little extra explanation other than  $C$  is an area ratio, while  $\mathcal{R}$  is a linear ratio of the radii of the inscribing to circumscribing circles (see above).

## APPENDIX B: VOLCANIC INTRUSIONS

### B1 Modelling intrusion spread—assumptions

The radial spread of an idealised volume of material is modelled assuming material is forced upwards high into the atmosphere and spreads at the neutral buoyancy level with initial conditions:

- An atmosphere at rest. No vertical wind shear and no horizontal advection.
- The volume is axially symmetric, conserved and has the idealised shape of a torus or an ellipsoid.
- The initial impulse is discrete: it can be specified by a single volume flux (flow rate)  $Q_0$  ( $\text{m}^3 \text{s}^{-1}$ ) or with a slow exponential rate of decay with time.
- The height of the intrusion is small compared to the depth of the atmosphere and can be modelled as an isolated “hump”.

To calculate how the radius spreads with time when both  $r$  and  $h$  are functions of time, an idealised shape for the material volume is assumed. The volume of an ellipsoid with radius  $r$  and height (depth),  $h$  is:

$$V_e = \frac{4}{3}\pi r^2 h. \quad (\text{A1})$$

The volume is one third larger than the volume of a cylinder with the same height and radius, but the ellipsoidal shape is more realistic than a cylinder because the leading edge is sloped rather than sharp.

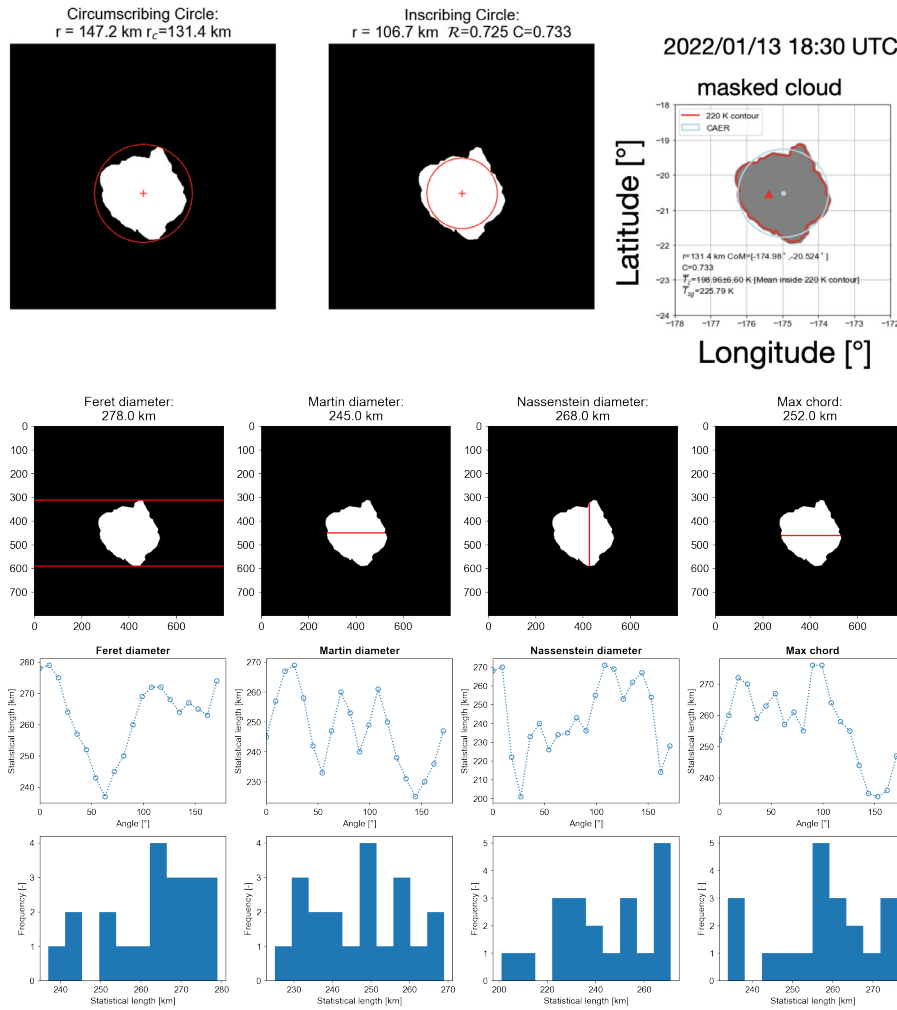


Figure A2: Shape metrics used to determine the morphology of the umbrella cloud contour. This example is for the 13 January 2022 eruption of Hunga. (Analyses performed using the Python `imea` package Kroell [2021].)

The volume of a torus with radius  $r$  and height (depth),  $h$  is (see Figure A4):

$$V_t = \frac{1}{2} \pi^2 h^2 r. \tag{A2}$$

The volume changes with time according to:

$$\frac{dV}{dt} = Q_0 \exp(-\alpha t), \tag{A3}$$

where  $Q_0$  is an initial flux ( $\text{m}^3 \text{s}^{-1}$ ) and  $\alpha$  is a positive inverse time constant.

**Torus**

A torus may be an appropriate shape for the spreading of the leading edge of the intrusion. Assume that

$$h = h_0 \operatorname{sech}(\omega t), \tag{A4}$$

where  $\omega$  is a non-zero, positive frequency that governs the spread of the 'hump'\* with time  $t$ . A motivation for assuming this form is based on the speculation that the leading edge

is behaving like a wave-like structure obeying weakly nonlinear dynamics, similar to solutions of the Korteweg-De Vries equation. Using Equation A2 and Equation A3:

$$\pi^2 \left[ r h \frac{dh}{dt} + \frac{1}{2} h^2 \frac{dr}{dt} \right] = Q_0 \exp(-\alpha t). \tag{A5}$$

Then,

$$\frac{dr}{dt} = 2 \left[ \frac{Q_0 e^{-\alpha t}}{\pi^2 h_0^2 \operatorname{sech}^2(\omega t)} + r \omega \tanh(\omega t) \right], t > t_0, \tag{A6}$$

$$\frac{dr}{dt} \approx \frac{2Q_0}{\pi^2 h_0^2}, 0 > t \leq t_0,$$

Written in the form

$$\frac{dr}{dt} + r \zeta(t) = \eta(t), \tag{A7}$$

the integral of Equation A7 can be evaluated by introducing the integrating factor,  $\xi(t)$ :

$$\frac{d(r\xi(t))}{dt} = \xi(t)\eta(t), \tag{A8}$$

\*It is possible to repeat the analysis with different functional forms for the hump, e.g.  $\operatorname{sech}^2(\omega t)$ .

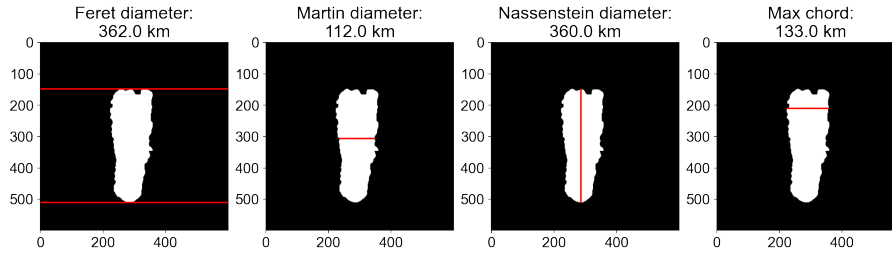


Figure A3: Morphological properties of the Taal eruption at 12:00 UTC on 12 January 2020.

where,

$$\begin{aligned}\xi(t) &= \exp \left[ - \int \zeta(t) dt \right], \\ \xi(t) &= \operatorname{sech}^2(\omega t), \\ \zeta(t) &= 2\omega \tanh(\omega t), \\ \eta(t) &= \frac{2Q_0 \exp(-\alpha t)}{\pi^2 h_0^2 \operatorname{sech}^2(\omega t)}.\end{aligned}$$

Integrating Equation 8 with respect to time and evaluating the constant of integration, assuming  $r = 0$  at  $t = 0$ , the result is:

$$r = \frac{2Q_0}{\pi^2 h_0^2 \alpha} \cosh^2(\omega t) [1 - \exp(-\alpha t)]. \quad (\text{A9})$$

Note that the same result can be obtained by integrating Equation A3 with boundary conditions and substituting from Equation A2 and Equation A4.

#### Ellipsoid, $V_e$

Only the upper half of the ellipsoid is considered assuming that the central plane (X-Y) of the ellipsoid is at  $h = 0$ , the neutral buoyancy level.

$$\frac{2}{3}\pi \left[ 2rh \frac{dr}{dt} + \pi r^2 \frac{dh}{dt} \right] = Q_0 \exp(-\alpha t) \quad (\text{A10})$$

If  $h = \text{constant}$  at  $t \sim 0$ , then this leads immediately to the solution,

$$v_r = \frac{dr}{dt} = \frac{3Q_0}{4\pi r_0 h_0}, \quad (\text{A11})$$

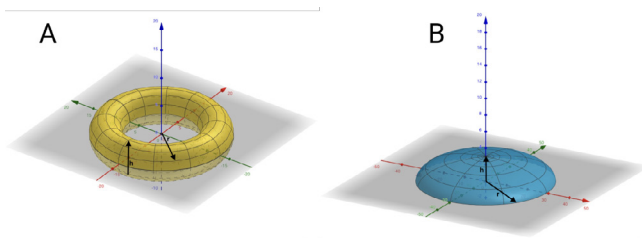


Figure A4: Torus [A] and Ellipsoid [B] volumes for the idealised shape of a spreading intrusion. The radial spreading occurs in the x-y plane while the decay of the height of the intrusion is in the z-direction. For the torus,  $h$  measures the diameter of the circular cross-section of the torus, while for the ellipsoid  $h$  is the height of the ellipsoid at the origin.

where  $h_0$  is the constant intrusion depth and this can only be true for  $0 < t < t_0$  and  $t_0$  is  $\sim O(3/N_f)$ ,  $N_f$  is the Brunt-Väisälä frequency [Rooney and Devenish 2014]. At these small times  $Q \approx Q_0$  and the ellipsoid has radius  $r_0$ . Thus as soon as the erupting volume reaches the neutral buoyancy level and begins to spread it is possible to estimate the initial flux from a measurement of  $r_0$  (by satellite) with an assumption only on  $h_0$ . Expanding Equation A10,

$$\begin{aligned}\frac{dr}{dt} &= \left[ \frac{3Q_0 e^{-\alpha t}}{4\pi h_0 r \operatorname{sech}(\omega t)} + 2r\omega \tanh(\omega t) \right], t > t_0, \\ \frac{dr}{dt} &\approx \frac{3Q_0}{4\pi h_0 r_0}, 0 < t \leq t_0.\end{aligned} \quad (\text{A12})$$

Making the substitution  $y = r^2$  leads to another general linear differential equation in the form of Equation A7 and an integrating factor,  $\xi(t) = \operatorname{sech}^4(\omega t)$ . This requires evaluating the integral,  $\int e^{-\alpha t} \operatorname{sech}^3(\omega t) dt$ , which involves the hypergeometric function. The form of the solution, which can be written down, is long, complicated and uninformative and as the torus model has been shown to match the data better than the Ellipsoid model, this solution has not been explored.

#### B2 Model results

The models are compared with values of  $h_0$ ,  $Q_0$ ,  $\alpha$  and  $\omega$  set to give a 'best' fit with the data for the eruption of Taal which lasted for  $\sim 7$  hours (see Figure 8O, which shows the radius is still increasing after  $\sim 5$  hours). Figure A5 shows the results. The parameters were evaluated to obtain fits that are similar whilst also giving the same volumetric flux,  $Q$ . The torus model appears to provide a better overall fit to the data than the ellipsoid model. To estimate  $Q_t$  from a model fit to the data the `Scipy curve_fit` package was used with bounds set and using `method='trf'`. It is apparent that  $Q_0$  and  $h_0$  cannot be estimated separately, only the term  $A = Q_0/\pi^2 h_0^2$  can be estimated, together with  $\omega$  and  $\alpha$ . The estimation process is done using all three parameters  $A$ ,  $\alpha$ , and  $\omega$  with bounds set to obtain a good fit (low residuals) and so that the variance on the coefficients (measured by  $\sqrt{\operatorname{diag}(\operatorname{cov})}$ ) is acceptable. The initial intrusion height,  $h_0$  must be prescribed in order to estimate  $Q_t$ . Webster et al. [2020] use a value of  $0.15H_T$  for the intrusion depth, where  $H_T$  is the height of the eruption column. This suggests that  $h_0$  is within the range 1.5–3 km for columns of 10–20 km high. Values for  $h_0$  are shown in Table 2; they range from 0.5–8 km for heights that range from 10–35 km. Constraining an accurate value for  $h_0$  is an issue and a source of error for estimating  $Q_c$  and  $Q_t$ . However,

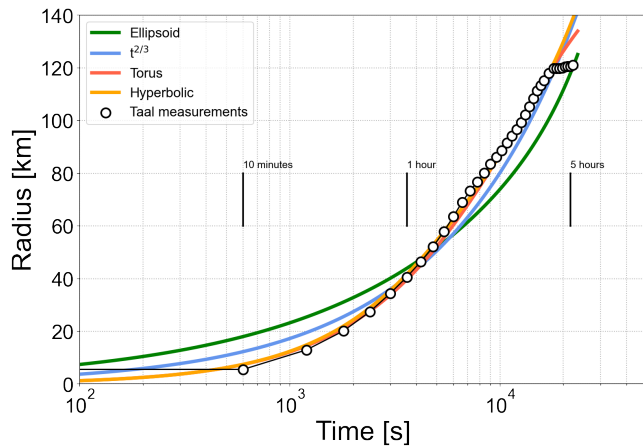


Figure A5: Model fits for the  $t^{2/3}$ , torus, hyperbolic and Ellipsoid models (solid lines) and Taal eruption measurements (circles) using appropriate values for model parameters.

the value of  $h_0$  must be consistent for the constant velocity and torus models and the fluxes estimated this way tend to be consistent (same order of magnitude) as the  $Q_{2/3}$  estimate from the  $t^{2/3}$  model, which does not depend on  $h_0$ .

### APPENDIX C: MODEL FITS MINIMISATION PROCEDURE

The parameters for each of the models were estimated using the Python `scipy optimise curve_fit` algorithm\*. For the  $t^{2/3}$  model this could be done either with a first guess or using bounds—both methods produced good fits with an acceptably low error covariance as there is just one parameter to estimate. As has been discussed, the  $t^{2/3}$  model is not applicable during later times, as the intrusion decelerates. Thus when the fits are evaluated against the measurements the biases and rms errors tend to be large. To quantify this,

\*[https://docs.scipy.org/doc/scipy/reference/generated/scipy.optimize.curve\\_fit.html](https://docs.scipy.org/doc/scipy/reference/generated/scipy.optimize.curve_fit.html)

the  $t^{2/3}$  fits were evaluated using the first  $n$  of the  $N$  ( $n < N$ ) measurements in each eruption sequence and also for  $n = N$ . For the hyperbolic and torus models the `curve_fit` procedure only produced low covariance errors when bounds were used, and these needed to be tight otherwise unreliable parameter estimates resulted. The likely reason for this is that there are too many free parameters in the models; as explained in the documentation this can be tested by examining the condition number of the covariance matrix. In order to reduce the number of free parameters in the torus model, we note that for this model at  $t = 0$ ,

$$v_r = v_{max} = \frac{A}{\pi^2}, \quad (\text{A13})$$

where  $A = Q_0/2h_0^2$  is a parameter to be estimated. In practice  $v_{max}$  is taken to be the largest  $v_r$  estimated from the data, but this is only an approximation since the temporal sampling may not be adequate to capture the true maximum velocity. The minimisation proceeds by setting  $A = \hat{A} = \pi^2 v_{max}$  and then varying  $\omega$  and  $\alpha$  in small steps to find values  $\omega_j$  and  $\alpha_j$ , that give minimums in,

$$r_{bias} = \frac{1}{n} \sum_{i=1}^n |r_i - \hat{r}_i|, \quad (\text{A14})$$

where  $n$  is the number of measurements,  $r_i$  is measurement  $i$  and  $\hat{r}_i$  is the model estimate, and

$$r_{rmse} = \sqrt{\frac{\sum_{i=1}^n |r_i - \hat{r}_i|^2}{n}}. \quad (\text{A15})$$

The  $\omega_j$  and  $\alpha_j$  are then input into the model and  $A$  is varied from  $\hat{A} - \delta\hat{A}$  to  $\hat{A} + \delta\hat{A}$ , where  $\delta\hat{A}$  is a small percentage ( $\pm 10\%$ ) of  $\hat{A}$ . The value of  $A$ ,  $A_j$  that gives a minimum in  $r_{bias}$  is taken as optimal. By construction  $A_j$ ,  $\omega_j$  and  $\alpha_j$  give the best fit of the model to the measurements, and the minimisation procedure provides bounds on their values.